International Journal of Biological Macromolecules 317 (2025) 144741

Contents lists available at ScienceDirect

International Journal of Biological Macromolecules

journal homepage: www.elsevier.com/locate/ijbiomac

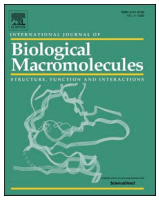

Towards a universal size distribution in a polymer network. Implications for drug delivery and plasmonic nanoparticle transport phenomena in polysaccharide and synthetic hydrogels

Stefano A. Mezzasalma [a,b], Michela Abrami [c], Gabriele Grassi [d], Mario Grassi [c,*]

[a] Materials Physics Division, Ruder Boskovic Institute, Bijenika cesta 54, 10000 Zagreb, Croatia
[b] Institute for advanced Neutron and X-ray Science (LINXS), Lund University, Ideon Building, Delta 5, Scheelevagen 19, 223 70 Lund, Sweden
[c] Department of Engineering and Architecture, Trieste University, via Valerio 6, I-34127 Trieste, Italy
[d] Clinical Department of Medical, Surgical and Health Sciences, Cattinara University Hospital, Strada di Fiume 447, I-34149 Trieste, Italy

ARTICLE INFO

Keywords:
Hydrogel and polymer networks
Non-Gaussian distribution
Low–field NMR
Rheology
Mesh size distribution
Drug diffusion
Statistical mechanics modelling
Nanoparticle transport phenomena

ABSTRACT

Polymeric hydrogels are paramount to outstanding applications in materials science, biology, medicine, pharmacy. Their similarity to living tissues is leveraged in clinical branches (oncology, cardiology, immunology, neurology, wound healing) for delivering a large range of drugs (encompassing DNA, RNA, protein molecules) and realizing in-vivo models of stimuli-responsive or controlled drug release. Rubber elasticity theory and the swollen network hypothesis are key for properly designing the geometric and mechanical features of hydrogels and polymer networks. The assumption of a Gaussian distribution of end-to-end lengths in a polymer molecule, however, can break down in several cases. Here, strongly supported by Low field NMR and rheology experiments, we propound the generalized Weibull law of extreme value statistics (EVS) to have universal validity in hydrogel materials. Mesh size values that account for an intrinsic statistical dependence between monomeric positions (or stiffness) show much better agreement with measurements conducted on physically crosslinked samples (agar, alginate and scleroglucan), including sputum specimens (rich in mucins) from patients affected by chronic respiratory conditions (cystic fibrosis) and on chemically crosslinked samples (poly-vinylpyrrolidone, PVP; poly-(ethylene-glycol/propylene-glycol), PEG/PPG). Across all ten gels, the Gaussian distribution yields the smallest average mesh size, ranging roughly from 7 nm for the densest alginate 2 % (9 gL^{-1}) hydrogel to about 80 nm for one of the sputum. Working with the pierced Gaussian inflates the mesh size to ≈1.5 × the Gaussian value, with increases from a modest +4 % in alginate 1 % up to nearly +100 % in the open PVP network (48 → 98 nm). The generalized Weibull distribution usually falls between the two Gaussians, yet in agar 1 % and scleroglucan 2 % it overtakes the pierced Gaussian (e.g. 20.2 > 15.8 nm for agar 1 %), reflecting a strong heavy-tailed distribution. The predicted mesh order therefore is Gaussian < generalized Weibull ≈ pierced Gaussian, with the precise ranking ruled by the width and skewness of each network statistics. Overall, our findings – being straightforward to apply – will profoundly impact on the description, conception and control of polymer networks, which often demand advanced instrumental techniques for compensating the lack of adequate predictive models. Among other relevant implications, aside from drug delivery, we highlight the characterization of the photothermal (or thermoplasmonic) response of hydrogel matrices hosting metal nanoparticles (e.g. with applications in hyperthermia cancer treatment and enhanced chemical processes). On the theoretical side, we emphasize the study of transport and thermomechanical properties of polymeric networks.

1. Introduction

A favorable matching among biocompatibility, mechanical and physicochemical properties make hydrogels particularly appealing in a wide range of life science applications, such as drug and gene delivery [1,2]. Release patterns and biodistribution of drugs can be ruled by convective effects when relevant swelling or osmotic pressures take place (e.g. in microporous membranes), otherwise diffusion is normally

* Corresponding author.
E-mail address: mario.grassi@dia.units.it (M. Grassi).

https://doi.org/10.1016/j.ijbiomac.2025.144741
Received 16 December 2024; Received in revised form 16 May 2025; Accepted 26 May 2025
Available online 28 May 2025

prevailing or rate-determining [3]. The mesh length scale, generally ranging in [1] (5–100) nm, can change with either the network architecture, the polymer or cross-linker concentrations, with hydration and external stimuli (e.g. temperature or pressure). Being a measure for the free space among adjacent strands in both cross-linked and entangled systems, it sets the steric hindrance [4] between drug and polymer chains. Hydrolytic or enzymatic network degradation/erosion (in bulk or at the surface), swelling processes governed by stimuli-responsive polymers (sensing changes of temperature, pH, glucose or ionic concentration, light properties, etc.), mechanical or magnetic field-induced deformations – are all size exclusion phenomena in "smart" hydrogels in response to a modulation of the mesh dimension or external stimulus [5–8].

Despite the apparent simplicity, it is arduous to understand precisely what characteristic length should be assumed as mesh size in a heterogeneous or imperfect system, containing chain distributions with high stiffness variability [9], dangling chains, closed loops, defects [10], etc. The mesh radius for instance – the mean end-to-end distance of polymer strands between cross-link points – can differ markedly from the network correlation length in the same hydrogel matrix [5]. Indirect mesh descriptions are carried out by diffusion, rheological, swelling and mechanical theories. Direct observations – by electron (EM), atomic force (AFM) and confocal laser scanning microscopy (CLSM), small-angle X-ray (SAXS) and small-angle neutron scattering (SANS) – are normally more reliable, but can damage the sample morphology (EM), have limited supra-micron resolution (CLSM), etc. [1] Indirect tests often suffer from neglecting topological effects, which get crucial when the solute and mesh are nearly equally sized. Influences of matrix topology and junction functionality, internal disorder and fluctuations, shapes of solute and solvent molecules – are unsatisfactorily treated by mesh size models, whose outcomes usually disagree with the observation and/or the quantities obtained as indirect estimates (solute diffusivity, Young's or shear moduli, etc.) [5,11]. Therefore, so far, there is by no means any universal mesh theory.

Advances in elasticity theories of rubbery solids (e.g. affine or phantom models [12]) led over the years to notable progresses in the mechanics of soft solids, where mesh and persistence lengths control both the linear and nonlinear mechanical response [13]. Two such classes of materials, however, do not always share the same mechanical behavior, raising the need for new fundamental views [11]. This intrigue deepens further in the biomechanics of soft tissues [14], where their response is intricately linked to specific biological functions [15]. Besides, while the mechanical strength usually augments with shortening the mesh size, stress relaxation may aid extracellular vesicles to overcome their confinement in the intercellular matrix by triggering fast anomalous transport [16]. Thus, it is clear how a precise determination of the mesh length scale(s) is vital for tailoring the most effective trade-offs among biological, mechanical and physico-chemical characteristics.

To improve the shortcomings of any (dominant) theory, one should not be tied down by old concepts or formulations. An incisive way to proceed is going to the heart of the three-fold connection of swollen polymer materials with a.) rubber-like elasticity, b.) mesh size and c.) swelling in a solvent – named "swollen polymer network hypothesis" [5] – and relaxing or even explicitly breaking the Gaussian hypothesis for the probability distribution of cross-link distances [17]. Ideal Gaussian models admit simple analytical solutions at the cost to sensibly affect their quantitative accuracy, they are broadly descriptive but hold in special cases (see the bibliography for the Introduction in our previous work [18]). We have therefore two main options: 1.) to abandon any claim to universality and regard different possible distributions in each system; 2.) to seek a new universal statistical measure for real polymer networks. The first is the subject of a recent comparison between Flory's assumption and three probability densities (Laplace, Cauchy, continuous Poisson), which shows that the best distribution in agar, alginate, scleroglucan hydrogels is never Gaussian [18]. The second option is focused on in the following, where a generalized Weibull function for extreme value statistics (EVS) and/or correlated random sums (i.e. global observables) is put forward [19,20].

Entropy defines a large fraction of many specific macromolecular properties, both synthetic and biological. Now, this paradigm shift, Gaussian → Weibullian, places for the first time the conformational statistics of hydrogel materials in a wider thermodynamic EVS (or Gumbel-like) universality class – comprising fluctuations in turbulent flows or plasmas [21], magnetic O(2) models [22], Bose gases [23], self-similar processes [24], $1/f\alpha$ noise [25], liquid crystals [26], and glassy matrices [27]. It will shed new light on the greatest open questions in the field (swollen polymer network hypothesis in life sciences, roles of topology, high-order interactions, etc.) and will have sizable consequences for modelling the next generation of precision hydrogels (for instance, in the context of mechanobiology of cancer cells [28], as well as in light-driven autonomous actuators and hierarchical oscillatory systems [29,30], among others).

Interestingly, substituting the Gaussian end-to-end distribution with the more general Weibullian distribution introduces considerable mathematical complexity in derivation. However, this leads to a relatively simple theoretical outcome: a corrective term in Flory's theoretical relation that links the shear modulus to the crosslink density of the polymeric gel. This corrective term depends on the Weibullian parameters, which will be experimentally determined using Low-Field NMR to characterize the polymeric network within the hydrogel volume. To demonstrate the practical relevance of this work, we focused on three physically crosslinked hydrogels - agar, alginate, and scleroglucan polysaccharides extensively used in pharmaceutical and food industries. Then, two chemically crosslinked hydrogels were considered (polyvinylpyrrolidone and poly-(ethylene-glycol/propylene-glycol)). Finally, further samples consisting in the sputa of patients suffering from cystic fibrosis (CF), a common genetic disorder in Caucasian populations [31], will be considered. The inflammatory response connected to CF leads to the formation of a complex molecular network within the mucus, consisting of proteins, mucins, and biopolymers, simultaneously promoting bacterial infections and hindering the delivery of drugs to epithelial cells [32,33]. Our findings substantiate the idea that characterizing the sputum structure using a Weibullian approach provides a more precise description, thus potentially informing the search for more effective therapies for this life-threatening condition. Besides, a more thorough understanding of the conformational and elastic properties of hydrogels offers the potential for a deeper comprehension of processes hosted or facilitated by a polymer matrix. They include phenomena such as chemical reactions driven by light or plasmonic nanoparticles in a soft phase (e.g. nucleation & growth or other photochemical or thermoplasmonic processes), an area of focus for one of our laboratories involved in an ongoing international project.

In summary, the aim of this paper was to improve upon classical theoretical predictions (i.e. Flory's) to enable a more accurate quantitative evaluation of the conformational statistics and nanostructure of polymer networks. This has significant implications for various hydrogel applications – from controlled drug release to their use as smart materials and in advanced technologies, such as nanoplasmonic nanoparticle matrices for photothermal heating.

2. Statistical mechanics model

Although the full details of the developed mathematical model are provided in the Supporting Information (SI 1–3), a summary of the key aspects is presented here. According to Flory theory [17], the probability (or statistical weight) Ω of a polymeric network undergoing a specific deformation is expressed as the product of two probabilities, Ω_1 and Ω_2. Ω_1 is related to the configurational entropy, relying on the probability distribution of random end-to-end chain vectors in the deformed state, $W = W(\mathbf{r})$ [17,34]:

$$\frac{1}{\nu}\ln\Omega_1 = \ln J + \iiint_{R^3} W(\mathbf{R})\ln\frac{W(r)}{W(\mathbf{R})}d\mathbf{R} \tag{1}$$

Here, ν is the constant number of cross-linked strands distributed in space, while J is the Jacobian determinant of the deformation gradient, mapping $\mathbf{R} = (X, Y, Z)$ into $\mathbf{r} = (x, y, z)$. In Cartesian coordinates, the undeformed and stretched states are related as $x_i = \alpha_i X_i$, with:

$$J = \prod_i \alpha_i \tag{2}$$

where $\alpha_i = \alpha_x, \alpha_y, \alpha_z$ are the elongation ratios of the homogeneous deformation. Ω_2, instead, represents the "perfect gas" term, and it is connected to the probability that the polymeric units designated for crosslinking occur in appropriate juxtaposition:

$$\frac{1}{\nu}\ln\Omega_2 = -\frac{1}{2}\ln J + \text{const} \tag{3}$$

Thus, the total entropy in Boltzmann units (k_B) becomes:

$$ln\Omega = \ln\Omega_1 + \ln\Omega_2 \tag{4}$$

In our previous work [18] we reconsidered cross-link fluctuations by refining the derivation of Ω_2.

Nevertheless, to focus on isochoric conditions (J = const), we omit the modified perfect gas term, applying Eq. (4) to systems at constant volume (V), often observed experimentally. A second assumption was that the distribution of the end-to-end distances complies with a perfect Gaussian pattern (see next Eq. (13)), which yields an entropy function per strand (s_g) quadratic in α_i (SI 1.1) [35]:

$$s_g\,(\{\alpha_k\}) \equiv \frac{1}{\nu}\,(\ln\Omega_{1n})_{T,V} = -\frac{1}{2}\sum_i \alpha_i^2 + \frac{3}{2} \tag{5}$$

Networks are assumed to be homogeneous and isotropic, undergoing uniform strain and formed by strands that follow the force-extension relations in uniaxial and pure shear geometries [36]:

$$E \approx \frac{f_\sigma}{\varepsilon} \quad f_\sigma = -\frac{\rho k_B T}{Q}\left(\frac{\partial s_g}{\partial \alpha}\right)_{T,V} \text{(uniaxial)} \tag{6}$$

$$G \approx \frac{\tau_0^g}{\gamma^s} \quad \tau_0^g = -\frac{\rho k_B T}{Q}\left(\frac{\partial s_g}{\partial \gamma^s}\right)_{T,V} \text{(pure shear)} \tag{7}$$

where E is the Young's modulus, G is the shear modulus, T is the absolute temperature, Q represents the swelling/shrinking ratio, ρ is the density of cross-linked strands in the undeformed state, $f\sigma$ is the uniaxial stress, τ_0^g is the shearing stress, α denotes the homogeneous uniaxial elongation coefficient, and γ^s is the shear strain, all considered in the low strain regime ($\alpha \approx 1$). When adapted for Gaussian statistics (denoted here by the suffix g), such equations yield the well-known Flory's result:

$$G = Q^{-\frac{1}{3}}\rho k_B T = \frac{1}{3}E \tag{8}$$

One of the goals in this analysis is to reformulate this framework for a polymer network governed by a statistics forbidding conformational degrees of freedom at low end-to-end distances. Specifically, we have studied a pierced Gaussian near the origin (see next Eq. (14)), considered as an ideal model (SI 1.2), and also averaged the results using a Maxwell-Boltzmann-type statistics (SI 1.3). We then examined the Weibull distribution, initially in its standard form (SI 1.4), and then generalized it by a positive parameter a (see next Eq. (16)) characterizing the statistical dependence between the random monomeric vectors (SI 1.5) [20,37].

All the formal details were consolidated into a single paragraph (SI 2), covering both cases of uniaxial deformation and shear geometries. The key step, clearly, is the derivation of the conformational entropy, which for the pierced Gaussian (s_h) and generalized Weibullian distribution (s_a) is, respectively, equal to:

$$s_h(\{\alpha_i\}) = \frac{s_g(\{\alpha_i\})}{[1-\Phi(q)]^3} - \frac{s_g(\{\alpha_i\})}{[1-\Phi(q)]^3}\Phi\left(\frac{q}{\alpha_x}\right)\Phi\left(\frac{q}{\alpha_y}\right)\Phi\left(\frac{q}{\alpha_z}\right) - \frac{q}{\sqrt{\pi}[1-\Phi(q)]^3}\times\left[\gamma_x^s \exp\left(-\frac{q^2}{\alpha_x^2}\right)\Phi\left(\frac{q}{\alpha_y}\right)\Phi\left(\frac{q}{\alpha_z}\right) + \gamma_y^s \exp\left(-\frac{q^2}{\alpha_y^2}\right)\Phi\left(\frac{q}{\alpha_x}\right)\Phi\left(\frac{q}{\alpha_z}\right) + \gamma_z^s \exp\left(-\frac{q^2}{\alpha_z^2}\right)\Phi\left(\frac{q}{\alpha_x}\right)\Phi\left(\frac{q}{\alpha_y}\right)\right] \tag{9}$$

and

$$s_a(\{\alpha_i\}) = \frac{\delta(a\delta-1)}{\Gamma_a \eta}\sum_{k=x,y,z} H_{ka}(\{\alpha_i\}) - \frac{\delta}{\Gamma_a \eta^{\delta+1}}\sum_{k=x,y,z} L_{ka}(\{\alpha_i\}) \tag{10}$$

with the functions H_{ka}, L_{ka} defined as:

$$H_{ka} = \int_{R\setminus C_k^+}\left(\frac{t-u}{\eta}\right)^{a\delta-1}\exp\left[-\left(\frac{t-u}{\eta}\right)^{\delta}\right]\ln\left(\frac{\alpha_k t-u}{t-u}\right)dt \tag{11}$$

$$L_{ka} = \int_{R\setminus C_k^+}\left(\frac{t-u}{\eta}\right)^{a\delta-1}\exp\left[-\left(\frac{t-u}{\eta}\right)^{\delta}\right][(\alpha_k t-u)^{\delta}-(t-u)^{\delta}]dt \tag{12}$$

Eq. (9) defines the dimensionless parameter q as a measure of the region inaccessible due to conformational constraints, with Φ denoting the error function. In the last three relations, u, η and δ are the (positive) parameters of the standard Weibull function, $C_k^+ = C_k^+(u)$ is the forbidden gap across the axis k, and Γ_a is the Gamma function evaluated at a. The link between conformational entropy and mechanical properties – namely Young's modulus and the shear modulus – is established assuming small engineering and shear strains, respectively (SI 2.3–2.4). The most important results are summed up here by two new relationships, Eqs. (15) and (17).

We note that applying our model to covalent crosslinking does not need any modification of the theory. A potential concern could be whether the second configurational contribution plays a different role, but within Flory's framework the answer is negative. For an isochoric system (J = constant = 1), the contribution of Ω_2 is zero. As previously discussed [18], this assumption is an approximation which may be affected by junction fluctuations. However, given the greater covalent strength of cross-links, they are expected to be more localized than in ionic hydrogels. Thereby, we will continue here referring solely to the Ω_1 configurational integral also for synthetic polymers.

2.1. Pierced Gaussian distribution

The first step we take in relaxing the Gaussian hypothesis is to exclude the most flexible degrees of freedom from the conformational statistics of the network (SI 1.1–1.3; 2.1–2.2), preventing polymer chains from attaining shapes with end-to-end distances that belong to a neighborhood of zero.

A simplest way to proceed is to 'pierce' the Gauss law by a gap of given width (u) around the origin, setting a sort of hard-sphere diameter or steric hindrance in the distribution. The conceptual validity of this elementary operation relies on a number of features typically met in real systems – excluded volumes (e.g. non-zero molecular diameters), topological interactions, defects – and can be given a microscopic interpretation, at the repeat unit scale (SI 3.2.1). It has the advantage to return an exactly solvable model with the relevant implication that follows. In Flory's configurational view, when the Cartesian coordinates $X_i \in \Re$ of end-to-end vectors $\mathbf{R} = (X, Y, Z)$ are normally distributed (Fig. 1A):

$$W_{gi}(X_i) = \frac{\beta}{\sqrt{\pi}}\exp(-\beta^2 X_i^2) \tag{13}$$

the spatial fluctuations of polymer distances, as determined by the radial distribution variance $\langle R^2\rangle = 3/(2\beta^2)$, play no role in the network elastic

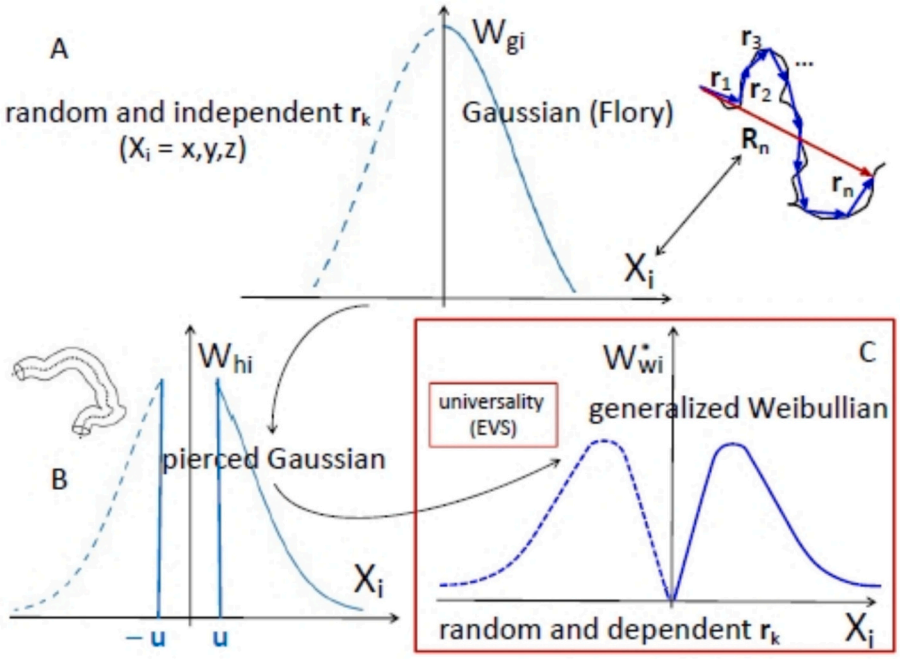

Fig. 1. Polymer end-to-end length distributions confronted in this work. **A**) The Gaussian Flory's hypothesis for the random sum of n monomeric vectors, $\mathbf{R}_n = \sum_{k=1}^{n}\mathbf{r}_k$. The displacement X_i is the $\mathbf{R}_n$ projection along the rectangular coordinate with unit vector $\mathbf{e}_i$ upon large unit numbers, $X_i = \lim n\to\infty\,(\mathbf{e}_i \bullet \mathbf{R}_n)$. **B**) 'Piercing' the Gauss distribution in a neighborhood of the origin (for simplicity, a symmetric gap of absolute value u in each coordinate) to disallow the most flexible conformational states. **C**) Generalized Weibullians give a more realistic account of finite size (and related) effects, remodelling the forbidden area by a continuous distribution of states and introducing a statistical dependence (or correlation) between monomeric segments. Weibull's aleatory variables (along with Gumbel's or Fréchet's) belong to a universal class known as Extreme Value Statistics (EVS).

response.

In our case, instead, we expect this fundamental property to be invalidated. Consider in fact a Gaussian law pierced at the origin of each space coordinate (Fig. 1B):

$$W_{hi}(X_i) = \begin{cases} \dfrac{\beta}{\sqrt{\pi}\,[1-\Phi(q)\,]}\exp\left(-\beta^2 X_i^2\right) \text{ if } X_i \notin (-uu) \\ 0 \text{ if } X_i \in (-uu) \end{cases} \tag{14}$$

Φ being a shorthand notation for the error function (erf), normalizing Eq. (14) to unity, and $q \equiv \beta u$ introducing a hindrance-fluctuation parameter, capturing the balance between steric obstruction and disorder in the spread of polymer lengths.

By replacing $W_g(\mathbf{R}) = W_{gX}(X)\,W_{gY}(Y)\,W_{gZ}(Z)$ with $W_h(\mathbf{R}) = W_{hX}(X)\,W_{hY}(Y)\,W_{hZ}(Z)$ in Flory's first integral, a new exact relation for uniaxial Young's (E_h) and pure shear (G_h) moduli is obtained for a pierced Gaussian network (SI 1.2). In an unswollen material (i.e. exhibiting a swelling ratio of unity, $Q = 1$), it is:

$$\frac{E_h}{E} = \frac{G_h}{G} = \frac{1-\Phi^3(q)}{[1-\Phi(q)\,]^3} + \frac{4q^2\Phi(q)\exp(-2q^2)}{\pi\,[1-\Phi(q)\,]^3} + \frac{4q^3\Phi(q)\exp(-q^2)}{\sqrt{\pi}\,[1-\Phi(q)\,]^3} \tag{15}$$

G and E being the Flory predictions in Eq. (8). Pure Gaussian responses are regained, $E_h \to E$ and $G_h \to G$, when chain molecules return to being fully unhindered ($u/\sigma \to 0^+$). In an alternative description, the hindrance-fluctuation parameter may be conceived as the absolute value of a vector random variable defined within the polymer matrix. A Maxwell-Boltzmann averaging of Eq. (15) for small enough values of q brings to a smoother functional dependence on the mean value $\overline{q} = (3/2)^{0.5}\,(\overline{u}/\sigma)$, valid both in unswollen and swollen ($Q \neq 1$) networks, which reads $E_h/E = G_h/G \approx (1-\overline{q})^{-2} \geq 1$. Deviation of this relation from Flory's theory follows a linear pattern multiplied by $(1-\overline{q})^{-2}$, and warrants individual discussion on a case-by-case basis. Whenever applicable, it offers the advantage of being significantly simpler than Eq. (15). To sum up, mechanical moduli coming from piercing the normal distribution reflect an intrinsic rigidity overlooked by seminal Flory's models, impacting meaningfully in mesh size calculations. We will prove how this feature recaptures a better agreement with hydrogel measurements.

2.2. Weibullian distribution

Pierced distributions have the clear drawback of demarcating the accessible conformational area ($|X_i| \geq u$) by an indefinitely sharp cut from the inaccessible gap ($|X_i| < u$). A more realistic yet similar probability density for a continuous random variable is the generalized Weibull's (Fig. 1C) [38]:

$$W^*_{wi}(X_i) = \frac{\delta}{\eta\Gamma_a}\left(\frac{X_i-u}{\eta}\right)^{a\delta-1}\exp\left(-\left(\frac{X_i-u}{\eta}\right)^{\delta}\right) \tag{16}$$

where the coefficients, all positive, are specific to each chemical system. They comprise the shape (δ), length scale (η) and correlation (a) parameters, with Γ_a representing the Gamma function calculated in a. Weibull's statistics disrupts the straightforward Gaussian response to changes in available conformations during chain extension, rendering calculations far less immediate. Yet, the standard law ($a = 1$) has already been used in hard materials and soft matter physics. As a size distribution (Rosin–Rammler law), it was applied to crushed particles and connected with fragmentation principles [39]. A branching structure would be formed with particle numbers eventually reaching a geometric scale invariance (with fractal dimension obeying $-d_f/3 \sim \delta - 1$). A behavior similar to Weibull's was also discussed for a real self-avoiding chain with radius $\sim \eta$ in a good solvent [40]. In the scaling regime of large numbers of repeat units [41], it can be proven that chain entropy increase consistently with increasing δ, when $\delta > 1/\sqrt{a}$ (SI 3.1).

Notoriously Weibull's laws, along with Fréchet's and Gumbel's, can also model the asymptotic EVS fluctuations in a countable set of

independent, identically distributed aleatory variables with bounded, power-law and exponential tails, respectively [42]. Later extensions of these models aimed to explore the resemblance between extreme value problems and the statistics of random sums of non-independent variables, with the coefficient $a > 0$ quantifying their dependency or correlation [19,20]. Eq. (16) can thus represent a polymer end-to-end vector (the global observable) that is built as a spatial sum of statistically dependent repeat unit positions within a large enough medium (i.e. the hydrogel, or polymer network). Imperfect materials exhibiting correlations along their backbone are a common occurrence. What stands out, however, is the discovery that their statistical distribution falls within the widespread EVS class, capable to pool a variety of disparate correlated or critical phenomena [21–27]. In these scenarios, fluctuations of global observables often converge to an asymmetric distribution, with an exponential tail on one side of it and a steep fall-off on the other [19]. In general, the value of a should decrease with increasing the ratio between statistical correlation length and system size [20]. The existence of (strong) statistical dependencies constrains this ratio to take a constant value in the thermodynamic limit, violating the central limit theorem (CLT). Obviously, not every correlated process is expected to obey a generalized EVS, but will need to be subjected to experimental verification. We have further developed a microscopic explanation for Weibull's statistics, detailing the intermolecular force fields it represents at the monomeric level (SI 3.2–3.3). While a combination of elastic and logarithmic potentials may formally provide a coherent framework (SI 3.2.2), definitive interpretations will necessitate additional experimental or computational investigations.

Eq. (16) does not allow to derive a closed-form expression of the final mechanical features, for a suitable expansion in powers of u/η is required. After prolonging it for continuity along the negative X_i-axis, our extended conformational calculus returns new simple formulas for Young's and shear moduli, i.e. (SI 2.3, 2.4):

$$\frac{E_w}{E} = \frac{G_w}{G} \approx \frac{1}{2} a \delta^2 Q^{\frac{\delta-2}{3}} \left(1 + \frac{u}{\eta} Y_a\right) \quad (a > 0) \tag{17}$$

The perturbation term Y_a (δ, Q) consists of a nontrivial dependence on the swelling ratio (Q), shape and correlation parameters, whose analysis falls outside the scope of the present work. However, while we have reported a parametric discussion of it for a number of a, δ and Q values (SI 1.4, 1.5), it turns out $Y \to 0$ for an unswollen material ($Q = 1$) as $\delta \to 1^+$ (exponential limit) and $a \to 1$. It is finally noteworthy to confront Flory's result with Eq. (17) in the limit of Rayleigh's statistics ($\delta = 2$, $a = 1$), yielding stiffer networks with doubled moduli, $G_w/G \approx 2$.

3. Experimental

The first three samples considered in this paper consist of polysaccharides hydrogels (alginate, agar and scleroglucan) that find wide use in biomedical field for their peculiar properties such as biocompatibility and their ability to form strong and weak hydrogels under mild conditions [43]. The latter two samples derive from the sputum of cystic fibrosis patients, while the last two are prepared with *poly(vinylpyrrolidone)* and *poly-(ethylene-glycol/propylene-glycol)*, synthetic polymers widely used in the pharmaceutical field.

3.1. Materials

The *alginate* used in this paper (molecular weight $\approx 10^6$ Da), generously provided by FMC Biopolymer Ltd., UK, had a high GG content (≈70 % GG and 30 % MM). *Agar* (molecular weight $\approx 1.2 * 10^5$ Da), supplied by Biokar (Diagnostics, France), was of food grade, i.e. essentially composed of agarose. *Scleroglucan* (Actigum CS11, Cargill (Minneapolis, MN, USA)) average molecular weight was $1.2 * 10^6$ Da. The *poly(vinylpyrrolidone)* (PVP K90, molecular weight $\approx 3.6 \bullet 10^5$ Da) was supplied by Sigma Aldrich while the copolymer poly-(*ethylene-glycol/propylene-glycol*) (PEG-PPG) was synthesized as described in [44]. The two *sputum samples* considered here (samples CF167 and CF178) belong to those studied by Abrami and co-workers [32]. They were provided by the Burlo Garofolo Hospital (Trieste, Italy), following a procedure approved by the Ethics Committee (prot 000543, 17-02-2020, CEUR-2019-Em-408). A signed agreement was obtained from each patient.

3.2. Samples preparation

Alginate hydrogel was prepared by dispersing an appropriate amount of alginate powder into stirred distilled water at room temperature until a homogeneous solution formed (alginate mass fraction 0.01 and 0.02; % mass fraction = 1 and 2 %, respectively). Then, a suitable amount of alginate solution was poured into a flat-bottom beaker to form a film with a thickness approximately equal to 1 mm. Subsequently, a $CaCl_2$ water solution (Ca^{2+} concentration equal to 5 g/l for the 1 % alginate and 1, 3 and 9 g/l for the 2 % alginate) was rapidly sprayed on the gel surface to promote alginate crosslinking (volume of the sprayed crosslinking solution was approximately equal to the gel volume). After 5 min of contact, the crosslinking solution was removed and the crosslinked film was immediately and gently cleaned with laboratory paper. After formation, the gel was cut into 35 mm diameter disks (thickness ≈ 1 mm) using a stainless-steel punch of the same diameter as the rheometer sensor. For LF-NMR measurements, ≈8 mm diameter gel disk (≈1 mm thick) was inserted in the LF-NMR glass tube.

A*gar* hydrogel was prepared by dissolving 1 g of polymer into 99 g of distilled water at 90 °C, resulting in a 1 % polymer phase. The solution was homogenized and poured into vessels to induce gelation upon cooling at room temperature. For rheology characterization, the vessel was a cylinder ≈ 2 mm thick and ≈50 mm in diameter. The gel was formed, it was cut into disks 35 mm in diameter using the same procedure adopted for alginate gels. Before NMR tests, the solution was poured directly into the LF-NMR glass tube.

Scleroglucan hydrogel (polymer mass fraction 0.02; 2 %) was prepared by gradually adding the polymer powder to distilled water under mechanical stirring at room temperature. Just after preparation, the system was kept in a fridge at a temperature of 8 °C for 24 h in order to allow gel formation. Due to its weak nature, the gel could be easily placed in the rheometer sensor and the LF-NMR glass tube with the aid of a spatula.

While Alginate, Agar and Scleroglucan were physically crosslinked, *PVP-K90* and *PEG-PPG* underwent chemical crosslinking. In particular, *PVP* solution was prepared by dissolving the polymeric powder in a mixture of deionized water (99.1 % *v/v*) and H_2O_2 (0.9 % *v/v* – initiator), with a polymer concentration of 20 wt% under stirring (250 rpm) at 50 °C for 36 h. The solution was cast into a cylindrical mold (1 mm deep, 15 mm in diameter) and 0.5 mm thick glass discs were clamped onto the mold to prevent water evaporation during UV exposure (33 min exposure equivalent to 100 J) [45]. *PEG-PPG* hydrogel was synthesized by mixing the starting monomers (poly-(ethylene glycol)diglycidyl ether, 47.1 % wt; Jeffamine M600, 42.4 % wt; Jeffamine D400, 10.5 % wt) (JD400) at 80 °C, without solvents (JM600 and JD400 are PPG oligomers bearing one and two terminal amino groups, respectively). Subsequently, the mixture was poured into the cavities of silicone molds where chemical crosslinking took place at 80 °C for 45 h. The obtained bar-shaped specimens ($2 \times 7 \times 90$ mm^3) were purified by swelling in 2-propanol and finally equilibrated in NaCl 0.1 M [44]. Spontaneously expectorated (1–2 ml) *sputum* was collected from CF patients in sterile cups and immediately used for LF-NMR and rheological characterization.

As in complex molecular systems like those examined here each sample is inherently unique, only one sample per system has been considered.

3.3. Samples characterization

Samples characterization was performed at 25 °C (alginate 1 %, agar,

scleroglucan, PVP-K90 and PEG-PPG hydrogels) or 37 °C (alginate 2 % and sputum samples).

3.3.1. LF-NMR

The mesh size distribution of the studied hydrogels was determined by means of Low Field NMR looking at the magnetic relaxation of hydrogens belonging to water molecules trapped in the polymeric network. Accordingly, information on the polymeric network architecture (mesh size distribution) was indirectly gained by recording the effect of polymeric chains (solid component of the hydrogel) on the magnetic relaxation of water hydrogens. In the light of the very fast relaxation, the magnetic relaxation of hydrogens belonging to polymeric chains did not affect our measurements.

Water protons spin-spin relaxation time T_2 was measured by means of a Bruker Minispec MQ20 (0.47 T, 20 MHz, Germany) according to the CPMG sequence [46] sequence $\{90°[-\tau\text{-}180°\text{-}\tau(\text{echo})]_k\text{-}T_R\}$ with a 8.36 μs wide 90° pulse, $\tau = 250$ μs (time separation between the 90° and 180° pulses) and T_R (recycle delay) equal to 10s (see SI 5.1 for further details). Each sample was put inside a glass tube (internal diameter 0.008 m) that could be sealed by a proper plastic top just after sample insertion. Then, the glass tube was maintained at the set temperature (25 °C or 37 °C) for, about, 10 min before measuring. Finally, it was swiftly placed into the MQ20 sample holder, which is situated just above the magnetic field. The continuous T_2 distribution was determined by fitting the experimental FID ($I_s(t)$) by means of the following equation:

$$I(t) = \int_{T_{2min}}^{T_{2max}} a(T_2)\exp\left\{-\frac{t}{T_2}\right\}dT_2 \tag{18}$$

where T_{2max} and T_{2min} indicate, respectively, the lower and upper values of the continuous T_2 distribution, $a(T_2)$ is the unknown amplitude of the spectral component at the relaxation time T_2 while $\exp\{-t/T_2\}$ represents the decay term. In order to fit the experimental FID ($I_s(t)$) by Eq. (18), and get the continuous T_2 distribution (A_i vs T_{2i}), the following discretization was adopted [47]:

$$I(t) \approx \sum_{i=1}^{N} a_i \exp\left\{-t/T_2^i\right\}\left(T_2^{i+1} - T_2^i\right) = \sum_{i=1}^{N} A_i \exp\left\{-t/T_2^i\right\} \tag{19}$$

The T_2 distribution range ($T_{2min} - T_{2max}$) was sectioned logarithmically into $N = 200$ segments as a finer subdivision was found not necessary.

Because of the noise disturbing the measure of I_s, the fitting procedure must not minimize the χ^2 statistic, but a smoothed definition of it (χ_s^2) [47]:

$$\chi_s^2 = \sum_{i=1}^{N}\left(\frac{I_s(t_i) - I(t_i)}{\sigma_i}\right)^2 + w_{st}\sum_{i=1}^{N-2}\left|A_{i+2} - 2A_{i+1} + A_i\right|^2 \tag{20}$$

where σ_i represents the standard deviation of i^{th} datum, and w_{st} denotes the weight of the smoothing term (second summation in Eq. (20)) proposed by Provencher [48]. Although different criteria can be followed for determining w_{st}, we adopted the strategy proposed by Wang [49] according to which the correct w_{st} value is that occurring just below the heel (slope variation) of the function $\log(\chi_s)$ vs $\log(w_{st})$ (see further details in SI 5.4).

The continuous T_2 distribution can be transformed into hydrogel mesh size distribution by resorting to the Fiber-Cell [50] and Scherer theories [51]. To this purpose, recently, Abrami [52] demonstrated that, for a hydrogel polymer volume fraction $\varphi < 0.61$, the average mesh size ζ, deriving from the Scherer theory, can be properly approximated by:

$$\zeta = R_f\sqrt{\frac{C_1}{C_0}\frac{1 - 0.58\varphi}{\varphi}} \tag{21}$$

R_f being the radius of the polymeric chain (thought to be a long cylinder). Constants C_1 and C_0 depend on the mesh architecture ($C_1 = 1$ and $C_0 = 3\pi$ for a cubic mesh). In light of Eq. (21), the Fiber-Cell theory [50] leads to the following relation between ζ and the average value of the inverse of the relaxation time $(1/T_2)_m$ [53]:

$$\left(\frac{1}{T_2}\right)_m = \frac{1}{T_{2H2O}} + 2\frac{M}{\zeta\sqrt{\frac{C_0}{C_1}\frac{1-0.58\varphi}{\varphi}}} \tag{22}$$

$$\left(\frac{1}{T_2}\right)_m = \sum_{i=1}^{N}\frac{A_i}{T_{2i}} \tag{23}$$

in which T_{2H2O} is the bulk protons relaxation time (free water relaxation time. See SI 5.9 for further considerations on T_{2H2O} determination and on M (length/time) (SI 5.1), a physical parameter, called relaxivity, accounting for the effect of the surface of polymer chains on water proton relaxation. Indeed, M, dimensionally a velocity, expresses the ratio of the thickness to the relaxation time of the water layer surrounding to the polymeric chains surface [50]. Typically, in the case of polymer gels, M falls in the range 10^{-8}–10^{-5} m/s [44].

While Eq. (22) holds, on average, for all the polymeric network meshes, similar expressions can be written for meshes of different dimensions (ζ_i), by assuming the M independent of the mesh size [50]:

$$\frac{1}{T_{2i}} = \frac{1}{T_{2H2O}} + 2\frac{M}{\zeta_i\sqrt{\frac{C_0}{C_1}\frac{1-0.58\varphi}{\varphi}}} \tag{24}$$

T_{2i} indicate the relaxation times of water protons embedded inside polymeric meshes sized ζ_i. The bi-univocal correspondence between T_{2i} and ζ_i only holds in the fast-diffusion regime, i.e. when the mobility of water molecules, expressed by their self-diffusion coefficient D ($2.09 \bullet 10^{-9}$ m^2/s at 25 °C and $3.03 \bullet 10^{-9}$ m^2/s at 37 °C [54]), is large as compared to the rate of magnetization loss, identifiable with R_c M (i.e., $R_c\,M/D \ll 1$). In fact, in the slow diffusion regime, relaxation of all the water protons contained in the volume of a mesh of size ζ_i is not described by only one T_{2i} but a plurality of T_{2i}. R_c, indicating the radial distance from the polymer chain axis at which the effect of polymeric chains on water proton relaxation becomes negligible, can be expressed by [50]:

$$R_c = \frac{R_f}{\sqrt{\varphi}} \tag{25}$$

(see SI 5.1 for further considerations on the relations existing among M, R_c and R_f).

The combination of Eqs. (22) and (24) leads to the conclusion that the ratio (ζ_i^+) between ζ_i and its maximum value, ζ_{max}, depends exclusively on the relaxation times T_{2i} and T_{2max} (apart from the free water relaxation time T_{2H2O}):

$$\zeta_i^+ = \frac{\zeta_i}{\zeta_{max}} = \frac{\left(\frac{1}{T_{2max}} - \frac{1}{T_{2H2O}}\right)}{\left(\frac{1}{T_{2i}} - \frac{1}{T_{2H2O}}\right)} \tag{26}$$

Notably, Eq. (26), enables the relaxation times conversion into mesh size without requiring the R_f and φ knowledge, two values that, in many cases, are not easily determinable.

Accordingly, the probability $P_i(\zeta_i^+)$ of finding a mesh of size ζ_i^+ inside the polymeric network is given by:

$$A_i\left(\zeta_i^+\right) = A_i(T_{2i}) \quad P_i\left(\zeta_i^+\right) = \frac{A_i\left(\zeta_i^+\right)}{\sum_{i=1}^{N} A_i\left(\zeta_i^+\right)} \tag{27}$$

where $A_i(T_{2i})$ are known from Eq. (19) fitting to experimental relaxation data.

Starting from Eq. (27), it is possible to determine the end-to-end

distribution (F_{Si}) as detailed in Mezzasalma [18]:

$$F_{Si} \approx \frac{\sqrt[3]{A_i}}{\sum_{i=1}^{N} \sqrt[3]{A_i}} = \frac{\sqrt[3]{P_i}}{\sum_{i=1}^{N} \sqrt[3]{P_i}} \tag{28}$$

3.3.2. Rheology

The viscoelastic properties of our samples were determined by means of stress sweep and frequency sweep tests. Stress sweep tests were conducted applying a sinusoidal stress of constant frequency ($f = 1$ Hz) and increasing amplitude to detect the limit of the linear viscoelastic range. Frequency sweep tests, performed in the linear viscoelastic range, as to prevent any sample structure damaging, were carried out in the frequency range (10–0.01) Hz. The output of the frequency sweep tests, i.e. the elastic (G') and viscous (G'') moduli dependence on angular frequency ω (=2πf) (mechanical spectrum), was fitted by the generalized Maxwell model:

$$G' = g_E + \sum_{i=1}^{n_R} g_i \frac{(\lambda_i \omega)^2}{1 + (\lambda_i \omega)^2} \quad \eta_i = \lambda_i g_i \tag{29}$$

$$G'' = \sum_{i=1}^{n_R} g_i \frac{(\lambda_i \omega)}{1 + (\lambda_i \omega)^2} \tag{30}$$

where n_R is the number of Maxwell elements considered, whereas g_E (elastic constant of the purely elastic Maxwell element), g_i (i^{th} elastic constant) and λ_i (i^{th} relaxation time) represent model fitting parameters. Model fitting was performed assuming that λ_i were scaled by a factor 10 ($\lambda_{i+1} = 10\lambda_i$) [55,56]. The n_R determination was performed according to a statistical procedure, in order to minimize the product $N\chi^2$, where N indicates the number of fitting parameters and χ^2 is the sum of the squared errors [57]. The sample shear modulus G was evaluated as the sum of all g_i ($G = \Sigma g_i$) [58].

Rheological measurements were performed by means of a stress controlled rotational rheometer (Haake Mars III Rheometer, 379–0200 Thermo Electron GmbH, Karlsruhe, Germany) equipped with parallel plates geometry (PP35, gap of ≈(1 ÷ 2) mm, diameter = 35 mm, with serrated surfaces to avoid slippage at the wall) to characterize the alginate, agar, scleroglucan, PVP-K90 and PEG-PPG hydrogels. On the contrary, the two sputum samples were characterized by a cone and plate geometry (CP 35, diameter = 35 mm) due to their weak rheological nature. In all cases, the measuring device was kept inside a glass bell at saturated humidity conditions to avoid evaporation effects.

4. Results and discussion

4.1. Shear modulus determination

Figs. 2, showing the outcomes of the frequency sweep test referring to alginate 1 % 5 g/l and alginate 2 % 1 g/l, indicate the gel nature of these systems as both G' and G'' are parallel and G' is clearly prevalent over G''. Because similar qualitative considerations can be drawn for the sputum samples (Fig. 3), we can conlude that also these samples can be regarded as hydrogels even if the small values of both moduli (G', G'') and their dependence on ω collocate these systems inside the weak gels catergory. An inspection of SI. 5.3 section reveals that all other systems considered in this work are hydrogles, being alginate 2 % 9 g/l the strongest one. Generalized Maxwell model (Eqs. (29) and (30)) best fitting (solid lines in Figs. 2–3) allows us to conclude that the shear moduli of our systems are (see SI 5.3): G_{Agar}(Pa) = (3356 ± 104), $G_{Alg1\%}$ (Pa) = (8763 ± 166), G_{Sclg}(Pa) = (196 ± 7), G_{CF167}(Pa) = (21.5 ± 2.0), G_{CF178}(Pa) = (57.6 ± 2.3), $G_{Alg2\%\ 1g/l}$ (Pa) = (476 ± 7), $G_{Alg2\%\ 3g/l}$ (Pa) = (5447 ± 311), $G_{Alg2\%\ 9g/l}$ (Pa) = (20,709 ± 292), G_{PVP} (Pa) = (113 ± 13), $G_{PEG\text{-}PPG}$ (Pa) = (984 ± 242).

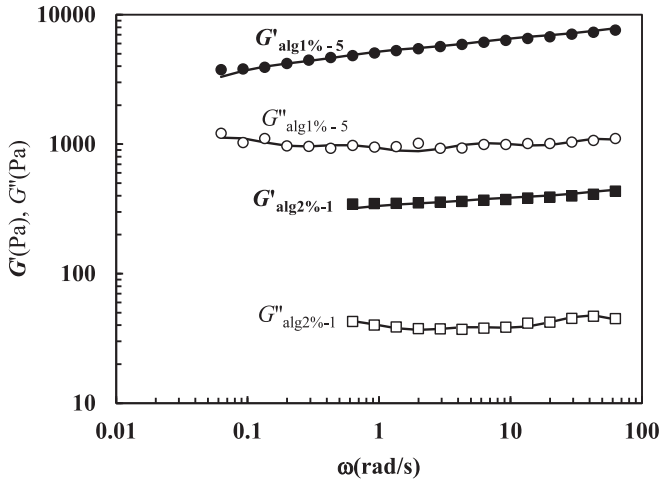

Fig. 2. Frequency sweep tests referring to alginate 1 % 5 g/l and to alginate 2 % 1 g/l. G' (closed symbols) and G'' (open symbols) are the experimental elastic and viscous moduli, respectively while f and ω (=2πf) indicate the solicitation frequency and angular frequency, respectively. The solicitation stress is equal to 2 Pa (see SI 5.3). Generalized Maxwell model (Eqs. (29) and (30)) best fitting is represented by solid lines.

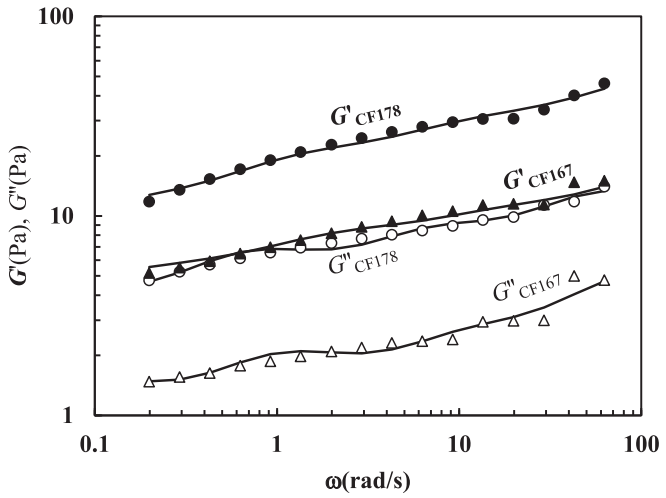

Fig. 3. Frequency sweep experiments for sputum samples CF167 and CF178. G' (closed symbols) and G'' (open symbols) are the experimental elastic and viscous moduli, respectively. f and ω (=2πf) indicate, respectively, the solicitation frequency and angular frequency. The solicitation stress is equal to 0.2 Pa (see SI 5.3). Generalized Maxwell model (Eqs. (29) and (30)) best fitting is represented by solid lines.

4.2. Determination of the end-to-end length distribution

Once the shear modulus has been experimentally evaluated, it is necessary to determine the end-to-end length distribution in order to properly apply our theory. For this purpose, Eq. (19) has been fitted to the experimental magnetic relaxation data depicted in (SI. 5.4) and referring to all samples considered. Fitting procedure led to the determination of the magnetic relaxation spectrum of the studied samples as reported in Figs. 4–5. Figs. 4–5 indicate that, except for the alginate 1 % and alginates 2 % 9 g/l cases, the fitting procedure relying on Eq. (19), provides a single-peak distribution spanning a range of values located far away from the free water peak (≥3000 ms; see SI 5.8). We can, therefore, conclude that the observed relaxation spectra actually belong to water molecules trapped inside the polymeric network. However, for the alginate 1 % and the alginate 2 % 9 g/l samples, the second peak,

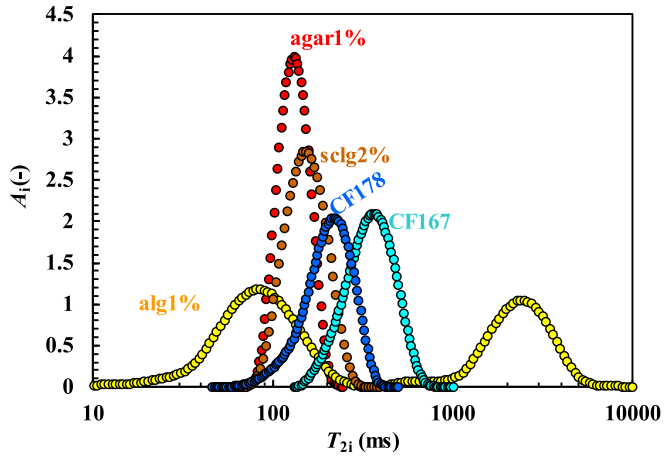

Fig. 4. Magnetic relaxation spectra (T_{2i}, A_i) referring to alginate 1 %, agar 1 %, scleroglucan 2 %, and sputum samples CF167 and CF178.

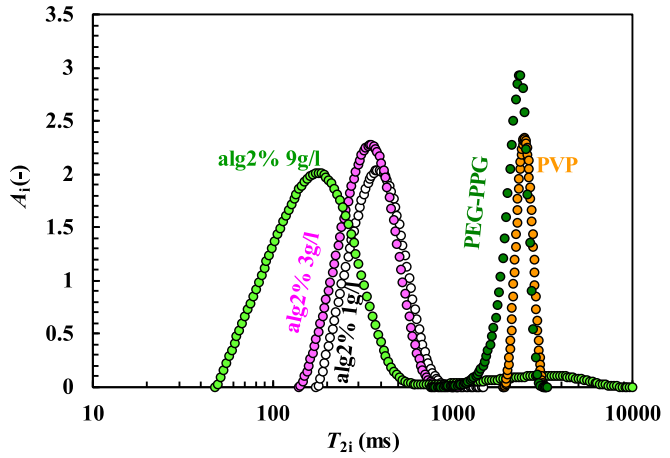

Fig. 5. Magnetic relaxation spectra (T_{2i}, A_i) referring to alginate 2 % (1,3 and 9 g/l), PEG-PPG and PVP.

occurring, respectively, at around 2800 ms and 3400 ms, corresponds to water accumulated outside the network. Indeed, it is well known that, after crosslinking, the alginate gel tends to contract by expelling water molecules (syneresis). Thus, it seems reasonable that syneresis occurred for the highest crosslinking agent ($CaCl_2$) concentrations considered (alginate 1 % 5 g/l; alginate 2 % 9 g/l). Accordingly, the first peak (occurring around 80 ms – alginate 1 % - and 200 ms alginate 2 % 9 g/l) can be regarded as the only one related to water immobilized inside the alginate network. For this reason, from now on, only the first peak will be considered for the alginate 1 % and the alginate 2 % 9 g/l hydrogels.

Relying on the relaxation distribution (T_{2i}, A_i) shown in Figs. 4–5, it is possible to obtain the end-to-end distribution. By setting T_{2H2O} = 3634 ms (25 °C) and T_{2H2O} = 4540 ms (37 °C) (see SI 5.9 for further details), Eq. (26) can convert the relaxation time (T_{2i}) into the corresponding (dimensionless) mesh size ζ_i^+, with a distribution of values (ζ_i^+, P_i), that can be determined as shown in SI 5.4.

Finally, Eq. (28) enables the determination of F_{si} so that the end-to-end distribution (ζ_i^+, F_{si}) can be derived as shown in Figs. 6–7 for two representative samples (scleroglucan 2 % and sputum sample CF167 – see SI 5.4 to see all other end-to-end distrubutions). In order to evaluate the ability of the different probability densities proposed in this paper, the Gaussian (Eq. (31)), pierced Gaussian (Eq. (32)) and the generalized Weibullian (Eq. (33)) functions have been fitted to the end-to-end distributions such those reported in Figs. 6–7. As 100• F_{si} denotes the percentage of end-to-end distances in the network, and the adopted

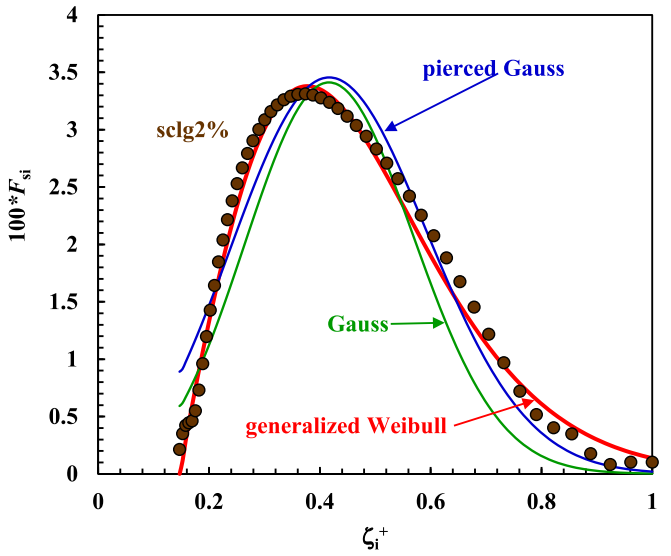

Fig. 6. End-to-end distributions (ζ_i^+, F_{si}) referring to scleroglucan 2 % (brown circles). Green, blue and red lines represent, respectively, the best fitting of the Gauss (Eq. (31)), pierced Gauss (Eq. (32)) and generalized Weibull (Eq. (33)) distributions.

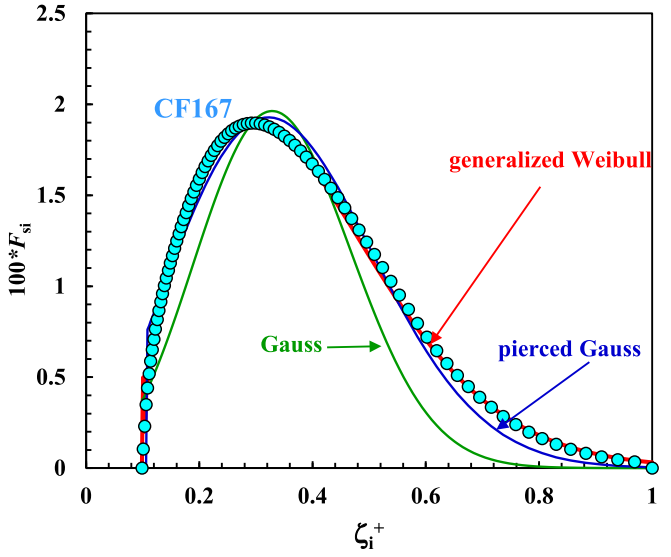

Fig. 7. End-to-end distributions (ζ_i^+, F_{si}) referring to sputum CF167 2 % (light blue circles). Green, blue and red lines represent, respectively, the best fitting of the Gauss (Eq. (31)), pierced Gauss (Eq. (32)) and generalized Weibull (Eq. (33)) distributions.

model functions return probability frequencies, the following expressions have been regarded for the Gauss, pierced Gauss and generalized Weibull distributions:

$$F_{Gi}\% = 100\left(\frac{\beta}{\sqrt{\pi}}\right)e^{\left(-\beta^2(\zeta_i^+-\mu)^2\right)}d\zeta_i^+ \text{ Gauss} \tag{31}$$

$$F_{Gpi}\% = 100\frac{\beta}{\sqrt{\pi}}\frac{1}{\left(1-\Phi\left(\beta\zeta_{\min}^+\right)\right)}e^{\left(-\left(\beta(\zeta_i^+-\mu)\right)^2\right)}d\zeta_i^+ \text{ pierced Gauss} \tag{32}$$

$$F_{Wgi}\% = 100\left\{\frac{\delta}{\eta\Gamma_a}\left(\frac{\zeta_i^+-\zeta_{\min}^+}{\eta}\right)^{a^*\delta-1}e^{\left(-\left(\frac{\zeta_i^+-\zeta_{\min}^+}{\eta}\right)^{\delta}\right)}\right\}d\zeta_i^+ \text{ generalized Weibull} \tag{33}$$

where $d\zeta_i^+$ is the dimensionless distance, evaluated on the horizontal axis, between two consecutive points reported in Figs. 6–7, μ and β are parameters of the Gauss (Eq. (31)) and Gauss pierced (Eq. (32)) distributions, ζ_{min}^+ is the minimum ζ_i^+ value considered by the Gauss pierced (Eq. (32)) and the generalized Weibull distribution (Eq. (33)), *a*, η and δ are generalized Weibull distribution parameters, Φ is a shorthand notation for the error function (erf) while Γ_a is the Gamma function with argument *a*.

An inspection of Figs. 6–7 reveals that all the three distributions can reasonably catch the experimental trends, even though it is clear that the best one is the generalized Weibull's and the Gaussian performs worse than pierced Gaussian (similar conclusions can be drawn for all other samples - see SI. 5.4). Such qualitative considerations are fully supported by the statistical parameters in Tables 1 and 2.

Indeed, while the *F*-test score indicates that all the three distributions considered can properly (from a statistical viewpoint) fit the end-to-end length data, the Akaike number [59] (see SI 5.4) suggests that the most probable distribution is the generalized Weibullian and that the pierced Gaussian is always to be preferred to the Gauss distribution. These evidences suggest that the stiffness and finite dimensions of polymeric chains cannot be neglected in real systems, leading to a more or less pronounced deviation from ideal behavior, which corresponds to the perfect Gaussian distribution and allows for the existence of vanishingly small meshes. In SI 3.4, we also discussed the Flory–Huggins parameter (χ_H) assumed by various polymer systems in water, which influence the enthalpy free function of the hydrogels. However, it is well known that macromolecular elasticity is predominantly entropic in nature. If experiments on the networks are conducted quickly relative to the time required for cross-link concentration changes due to chain deformations (with equilibrium typically reached on the order of hours [60]), any enthalpic contributions from chain segment interactions can be safely neglected in the former basic equations.

4.3. Mesh size distribution determination

Once the three functional forms (Gaussian, pierced Gaussian, generalized Weibullian) were tested to describe the end-to-end length distribution, one can estimate the average mesh size (ζ_m) of the polymeric network pervading the samples. This target is achieved by confronting the theoretical expressions of the shear modulus related to each distribution with its experimental value, determined by rheology measurements. Such relationships are given respectively in Eq. (8) (*G*), Eq. (15) (G_h) and Eq. (17) (G_w) where, for practical reasons, it is convenient to replace the density of crosslinks ρ in the reference state ($Q = 1$) with that corresponding to the rheological measurement conditions:

$$\rho_x = \frac{\rho}{Q} \tag{34}$$

relative to a swollen/shrunken sample ($Q \neq 1$). Thus, on the basis of the experimental knowledge of the shear modulus and the values of fitting parameters for the three distributions (Tables 1 and 2), the equations for *G*, G_h and G_w can be solved in the variable ρ_x.

The link between crosslink density (ρ_x) and average mesh size (ζ_m) is established by the equivalent network theory [61] (see SI 5.5) according to which the following relation holds:

$$\zeta_m = \sqrt[3]{6/(\pi \rho_x N_A)} \tag{35}$$

where N_A is the Avogadro number. Finally, from Eq. (26) and the definition of ζ_m, the maximum value of the network mesh size follows as:

$$\zeta_{max} = \zeta_m \frac{\sum A_i}{\sum \zeta_i^+ A_i} \tag{36}$$

which enables the conversion of dimensionless distributions into those carrying physical units (nm) (see Table 3), as shown in Figs. 8 (A-E) and 9 (A-E).

Regarding the systems considered in Fig. 8, remarkably, except for the alginate 1 %, where the mesh size distributions are similar for all three statistics, in the other cases the pierced Gauss and generalized Weibull functions result in values shifted towards larger mesh sizes compared to the Gaussian density. This is certainly plausible, given factors such as the stiffness and finite thickness of macromolecular chains, which make the formation of excessively small meshes improbable. Furthermore, for agar 1 % and scleroglucan 2 %, Weibull's statistics is manifested in a mesh size distribution that gets closer to the predicted average values coming from the LF-NMR theory (ζ_{mNMR}), developed for a cubic arrangement of meshes (Eq. (21) and SI 5.5) [52].

Table 1
Dimensionless parameters and statistical/physical quantities arising from best fitting the end-to-end length distributions with Gauss (β, μ), pierced Gauss (β, μ, ζ_{min}^+) and generalized Weibull (δ, η, ζ_{min}^+, *a*) functions. Statistical outcomes are summarized by the scores of the *F*-test and the Akaike numbers *AIC* (see SI 5.4).

	Alg2% 1g/l	*Alg2% 3g/l*	*Alg2% 9g/l*	*PVP-K90*	*PEG-PPG*
GAUSSIAN (Eq. (31))					
β (−)	4.90 ± 0.110	3.47 ± 0.112	4.37 ± 0.142	3.64 ± 0.059	4.70 ± 0.140
μ (−)	0.510 ± 0.006	0.148 ± 0.009	0.350 ± 0.007	0.326 ± 0.004	0.252 ± 0.006
F_{test}	$F(1,51,0.95) < 359$	$F(1,104,0.95) < 277$	$F(1,51,0.95) < 370$	$F(1,103,0.95) < 1540$	$F(1,87,0.95) < 343$
AIC	−124	−243	−93	−395	−235
Pierced GAUSSIAN (Eq. (32))					
β (−)	3.56 ± 0.098	3.41 ± 0.24	3.69 ± 0.15	2.83 ± 0.03	3.31 ± 0.10
μ (−)	0.492 ± 0.059	0.141 ± 0.022	0.324 ± 0.01	0.256 ± 0.004	0.166 ± 0.12
$100\ \zeta_{min}^+(-)$	(3.97 ± 0.63)	(0.91 ± 2.3)	(4.68 ± 1.0)	(8.87 ± 0.4)	(10.9 ± 1.0)
Q	0.141	0.031	0.173	0.251	0.359
σ	0.198	0.207	0.191	0.249	0.213
F_{test}	$F(2,50,0.95) < 411$	$F(2,103,0.95) < 144$	$F(2,50,0.95) < 269$	$F(2,102,0.95) < 6652$	$F(2,86,0.95) < 1159$
AIC	−161	−247	−120	−579	−406
Generalized WEIBULLIAN (Eq. (33))					
δ(−)	1.80 ± 0.08	1.35 ± 0.094	1.39 ± 0.106	2.40 ± 0.065	1.52 ± 0.091
η(−)	0.330 ± 0.015	0.356 ± 0.024	0.226 ± 0.029	0.454 ± 0.0067	0.259 ± 0.020
$\zeta_{min}^+(-)$	0.280 ± 0.003	$(8 \pm 0.2) * 10^{-3}$	0.150 ± 0.004	0.086 ± 0.0043	0.103 ± 0.003
a(−)	0.89 ± 0.073	0.66 ± 0.054	1.27 ± 0.205	0.523 ± 0.024	0.834 ± 0.115
Y_a	1.681	1.803	1.842	0.912	1.72
F_{test}	$F(3,49,0.95) < 1827$	$F(3,102,0.95) < 1211$	$F(3,49,0.95) < 1252$	$F(3,101,0.95) < 6510$	$F(3,85,0.95) < 1328$
AIC	−258	−541	−208	−724	−530

Table 2
Dimensionless parameters and statistical/physical quantities arising from best fitting the end-to-end length distributions with Gauss (β, μ), pierced Gauss (β, μ, ζ^{+}_{min}) and generalized Weibull (δ, η, ζ^{+}_{min}, *a*) functions. Statistical outcomes are summarized by the scores of the *F*-test and the Akaike numbers *AIC* (see SI 5.4).

	Alg2% 1g/l	*Alg2% 3g/l*	*Alg2% 9g/l*	*PVP-K90*	*PEG-PPG*
GAUSSIAN (Eq. (31))					
β (−)	6.9 ± 0.250	4.92 ± 0.172	5.52 ± 0.258	6.32 ± 0.310	9.18 ± 0.152
μ (−)	0.172 ± 0.005	0.233 ± 0.006	0.136 ± 0.007	0.215 ± 0.007	0.088 ± 0.002
F_{test}	$F(1,84,0.95) < 297$	$F(1,80,0.95) < 227$	$F(1,82,0.95) < 76$	$F(1,67,0.95) < 68$	$F(1,91,0.95) < 1910$
AIC	−181	−182	−144	−97	−203
Pierced GAUSSIAN (Eq. (32))					
β (−)	4.66 ± 0.184	3.46 ± 0.120	4.71 ± 0.470	3.77 ± 0.320	7.83 ± 0.320
μ (−)	0.101 ± 0.011	0.149 ± 0.012	0.099 ± 0.030	0.110 ± 0.033	0.069 ± 0.010
$100\zeta^{+}_{min}(-)$	(8.9 ± 1.1)	(10.8 ± 1.2)	(4.94 ± 3.0)	(12.9 ± 3.3)	(2.2 ± 0.9)
q	0.415	0.374	0.233	0.488	0.179
σ	0.152	0.204	0.150	0.187	0.09
F_{test}	$F(2,83,0.95) < 894$	$F(2,79,0.95) < 780$	$F(2,81,0.95) < 48.8$	$F(2,66,0.95) < 148$	$F(2,90,0.95) < 856$
AIC	−316	−329	−190	−169	−248
Generalized WEIBULLIAN (Eq. (33))					
δ(−)	1.21 ± 0.06	1.33 ± 0.026	0.99 ± 0.081	0.74 ± 0.036	1.01 ± 0.016
η(−)	0.146 ± 0.010	0.226 ± 0.007	0.145 ± 0.022	0.051 ± 0.007	0.059 ± 0.028
$\zeta^{+}_{min}(-)$	0.084 ± 0.001	0.105 ± 0.001	0.047 ± 0.003	0.130 ± 0.004	0.100 ± 0.007
a(−)	1.01 ± 0.067	0.907 ± 0.032	1.12 ± 0.120	2.1 ± 0.370	1.82 ± 0.760
Y_a	1.847	1.809	1.897	0.996	1.108
F_{test}	$F(3,82,0.95) < 1827$	$F(3,78,0.95) < 6524$	$F(3,80,0.95) < 352$	$F(3,65,0.95) < 3695$	$F(3,89,0.95) < 1363$
AIC	−631	−580	−522	−289	−542

Table 3
Estimations of the average (ζ_m) and the maximum (ζ_{max}) mesh size characterizing the polymeric network pervading the studied samples according to the three distributions considered.[a]

	Agar1%	*Alg1%*	*SCLG2%*	*CF178*	*CF167*
GAUSS					
ζ_m (nm)	13.3	9.9	34.0	51.4	80.4
ζ_{max} (nm)	24.7	39.4	88.8	132.8	273.0
Pierced GAUSS					
ζ_m (nm)	15.8	10.3	42.1	71.2	131.8
ζ_{max} (nm)	29.4	40.8	110.1	183.9	447.5
Generalized WEIBULL					
ζ_m (nm)	20.2	8.51	47.5	62.2	94.4
ζ_{max} (nm)	37.5	33.7	124.1	160.8	320.5

	Alg2% 1 g/l	*Alg2% 3 g/l*	*Alg2% 9 g/l*	*PVP-K90*	*PEG-PPG*
GAUSS					
ζ_m (nm)	25.8	11.4	7.3	48.0	35.4
ζ_{max} (nm)	142.0	34.6	40.2	186.5	1087
Pierced GAUSS					
ζ_m (nm)	46.5	19.2	9.9	98.0	44.2
ζ_{max} (nm)	255.7	58.2	54.1	380.8	1359
Generalized WEIBULL					
ζ_m (nm)	29.8	13.1	7.1	55.0	27.5
ζ_{max} (nm)	164.0	39.6	38.7	214.1	845.6

[a] *G* exact solution has been considered for ζ_m estimation (see Eq. (15)).

Regrettably, conducting a comparable analysis for the cystic fibrosis samples (CF-178, CF-167) is not feasible.

This limitation arises from the unknown polymer volume fraction and the challenging determination of chain radii, primarily due to the intricate topology of biomacromolecules, typically mucins, present in the surface layer of the airways. Nonetheless, the mesh size distributions depicted in Fig. 8D and E are entirely reasonable, falling within the typical pathological range spanning from a few tens of nanometers to approximately 300 nm, with a mean value of (145 ± 50) nm [62]. For the hydrogels shown in Fig. 9, the pierced Gauss distribution always results in values shifted towards larger mesh sizes compared to the Gaussian and the Weibullian density. In addition, the generalized Weibull distribution leads to larger mesh size with respect to the Gaussian except for the PEG-PPG hydrogel (Fig. 9E). This evidence is in agreement with our hypothesis about the role played by the stiffness and the finite thickness of macromolecular chains in preventing the formation of excessively small meshes. The suspicion that the pierced Gauss distribution excessively overemphasizes this aspect derives from the inspection of Fig. 10, showing a TEM picture of the PVP-K90 hydrogel.

Indeed, qualitatively speaking, we are tempted to affirm that meshes dimensions should be lower than approximately 150 nm, agreeing with the outcomes deriving from the Gauss and the generalized Weibull (Fig. 9 D) but not totally in accord with the outcomes of the pierced Gauss distribution predicting also the existence of larger meshes (up to ≈250 nm).

The inspection of panels *A*, *B* and *C* (alginate 2 % hydrogels) of Fig. 9 makes clear that the increase of the crosslinking agent concentration ($CaCl_2$) implies the shifting of the mesh size distribution towards smaller meshes, this being absolutely reasonable. While the Gauss and the generalized Weibull end-to-end distributions provide similar results, the pierced Gauss distribution is always associated to bigger meshes. Notably, the evaluation of the average mesh size (ζ_{mNMR}) according to the Low Field NMR approach (Eq. (21) and SI 5.5) does not vary with $CaCl_2$ concentration simply because this theory works only when crosslinking spontaneously occurs without the aid of the crosslinker. Thus, ζ_{mNMR} can change only upon the variation of the polymer concentration, the network topology and the radius of the network polymeric fibers.

The qualitative reliability of the developed approach, for what concerns alginate2%, is supported by the comparison of Fig. 9B (alginate 2 % 3 g/l) and Fig. 11, showing a TEM picture of alginate 2 % 3 g/l.

Indeed, the visual inspection of Fig. 11 reveals that, approximately, the network could be composed by meshes spanning in between ≈10–60 nm.

It is finally worth noting that the three-dimensional portrayal of the openings within the network, critical for drug diffusion (often the

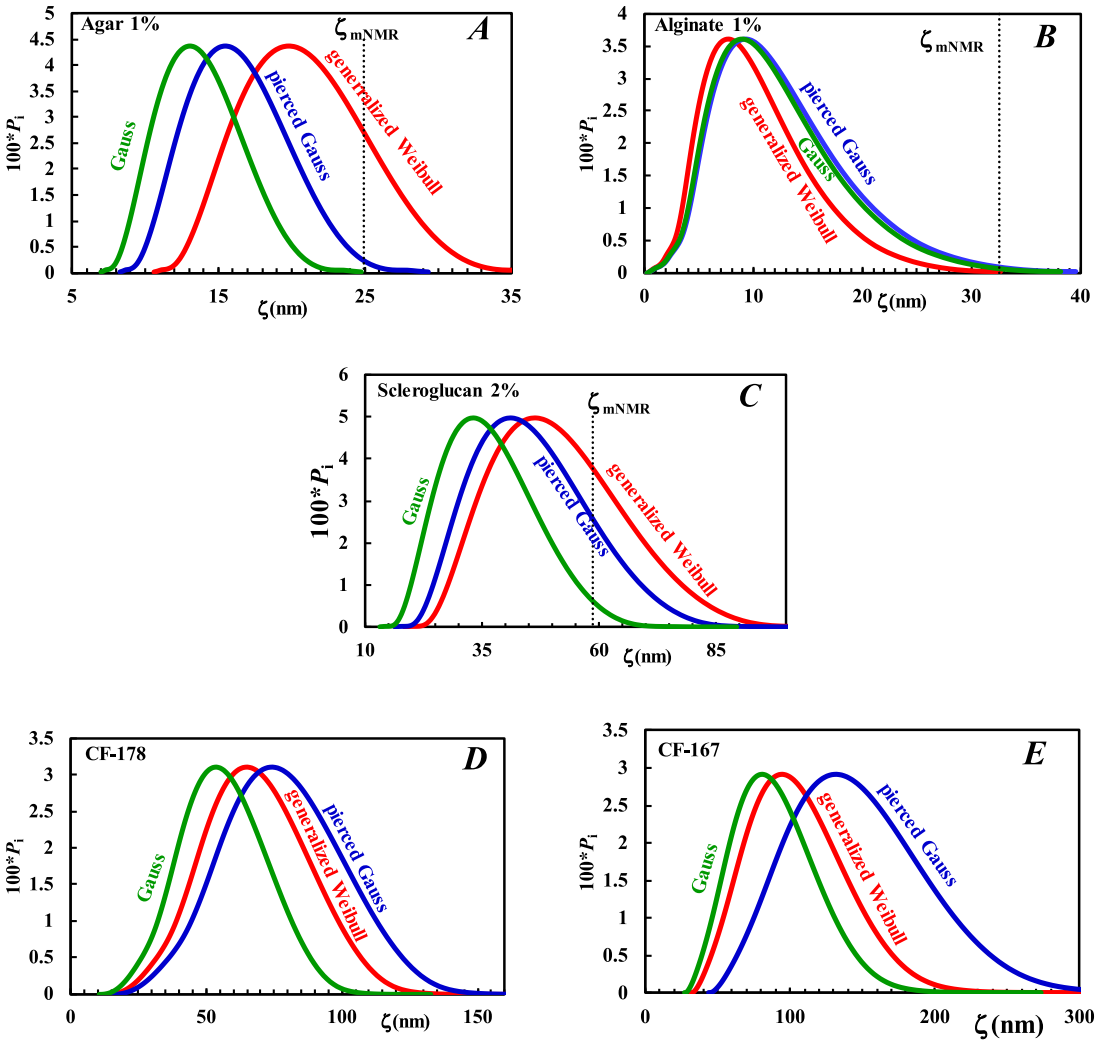

Fig. 8. Mesh size distributions, representing the (percentage) probability of encountering a (cubic) mesh of size ζ, are depicted for the first five samples under investigation. The green line corresponds to Flory's Gaussian assumption, while the blue and red lines illustrate the spread of mesh size values that result from the pierced Gaussian and generalized Weibull statistics for the end-to-end distances, respectively. Additionally, ζ_{mNMR} denotes the position of the average mesh size evaluated from the LF-NMR theory, assuming a cubic-like arrangement (Eq. (21) and SI 5.5). Panels **A** through **E** refer to agar 1 %, alginate 1 %, scleroglucan 2 % and cystic fibrosis hydrogels, CF 178 and CF 167.

primary resistance to mass transfer), is more accurately provided by the mesh size distribution – giving the likelihood of encountering a mesh of a specific mean size – than the end-to-end distance spread. This insight is underscored by our assessments of the mesh size distribution for agar 1 %, alginate 1 %, and scleroglucan 2 %, which closely align with the mean correlation length (ζ_c), a key metric for mesh size evaluation [5]. In contrast, they markedly deviate from the average end-to-end length (ζ_{ete}), which offers an alternative means to characterizing the network geometry (SI 5.8). These complementary length scales, along with the related shear moduli and crosslinking densities, are presented in SI 5.8 for agar 1 %, alginate 1 %, and scleroglucan 2 % hydrogels.

4.4. Impact in drug delivery and pulmonology: chronic respiratory diseases

A better characterization of a polymer network proves valuable in two therapeutic scenarios: when the hydrogel is employed for drug release and when the targeted biological system for therapy resembles a biopolymer network in structure. In the first framework, when regarding the most appropriate range of mesh sizes, it is crucial to evaluate the degree of geometric fluctuations and polymer mobility within the network. These elements are intimately connected to the chains' flexibility and elastic behavior [5]. Note that the comparison of the bare solute radius to the average mesh size is normally not applicable [65]. For small molecule drugs, which usually have molecular weights ranging from a few hundred to a few thousand Da, a mesh size approximately 2 to 10 times the size of the drug molecule could be suitable. Larger biological macromolecules like proteins, peptides and nucleic acids often necessitate larger mesh sizes to enable efficient diffusion. Mesh sizes ranging from 10 to 100 nm or more might be necessary depending on the macromolecular size. Proteins and peptides generally vary from a few to tens of nm, thus hydrogels with mesh sizes of (20–50) nm or larger could be appropriate. In the case of nucleic acids such as DNA or RNA, which can have lengths ranging from tens to hundreds of nm, even larger mesh sizes may be needed for effective diffusion. Therapies directed at specific tissues or cells might require further optimization of mesh size based on the target size features. For instance, if the target tissue possesses a porous structure with larger interstitial spaces, a hydrogel with a correspondingly larger mesh size might be necessary to facilitate drug penetration and distribution. Lastly, for controlled release applications aiming for sustained and controlled drug delivery, smaller sizes may be preferred to slow down diffusion and prolong release kinetics. Mesh dimensions ranging between (10–50) nm or smaller could be suitable for such applications.

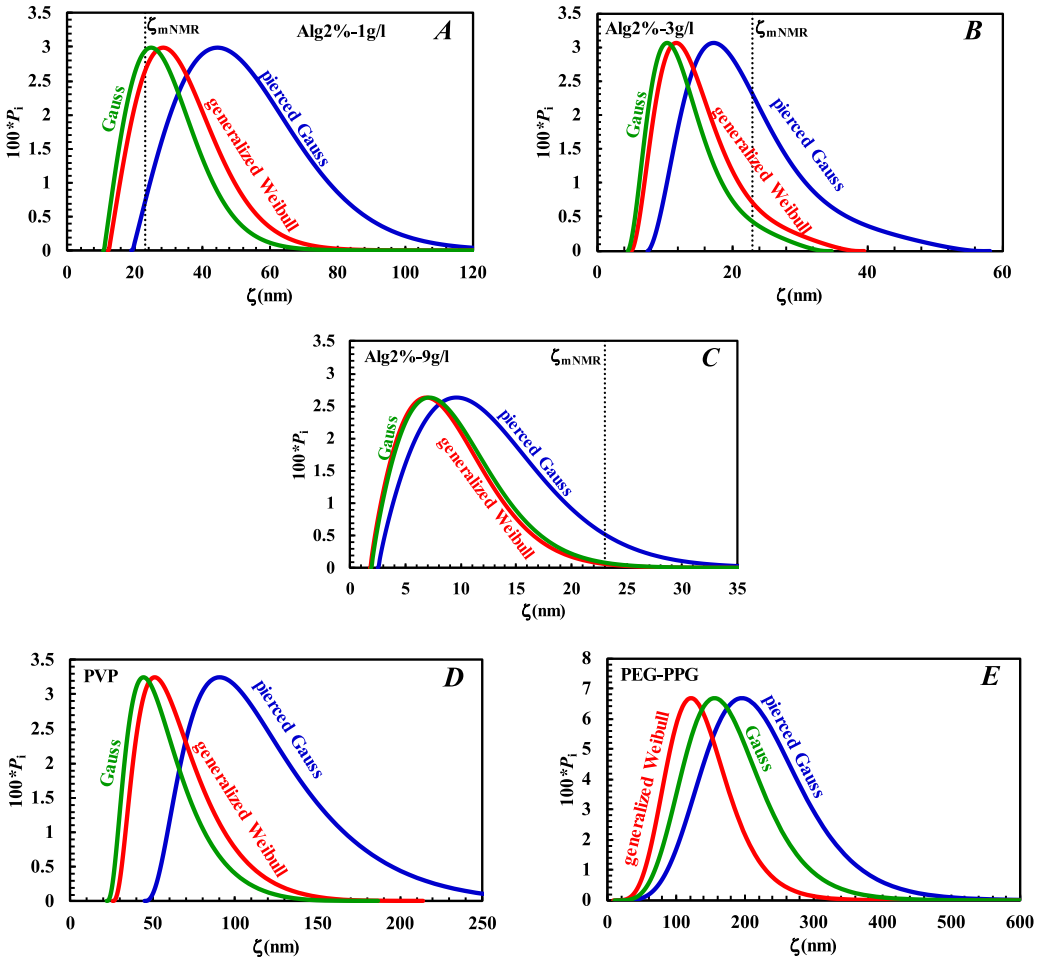

Fig. 9. Mesh size distributions, representing the (percentage) probability of encountering a (cubic) mesh of size ζ, are depicted for the second five samples under investigation. The green line corresponds to Flory's Gaussian assumption, while the blue and red lines illustrate the spread of mesh size values that result from the pierced Gaussian and generalized Weibull statistics for the end-to-end distances, respectively. Additionally, ζ_{mNMR} denotes the position of the average mesh size evaluated from the LF-NMR theory, assuming a cubic-like arrangement (Eq. (21) and SI 5.5). Panels **A** through **E** refer to alginate 2 % 1 g/l, alginate 2 % 3 g/l, alginate 2 % 9 g/l, PVP-K90 and PEG-PPG hydrogels.

The second scenario is addressed here to the context of pulmonary diseases. Inhalation stands out as a highly promising therapeutic strategy for delivering drugs to the lungs, addressing major diseases like cancer [66] and chronic respiratory conditions [67], including Cystic Fibrosis (CF, SI 4.4) [68], as well as asthma and chronic obstructive pulmonary disease (COPD). The benefits of local drug delivery to systemic administration are manifold, including the rapid degradation of therapeutics, the ability to circumvent systemic first-pass metabolism, the use of smaller therapeutic doses to achieve desired effects, the potential to mitigate nonspecific toxicity, the ability to target hard-to-reach regions of the lungs such as distal bronchi [69] and the versatility to administer various types of therapies ranging from traditional antibiotics, bronchodilators, anti-inflammatories to gene therapy agents (DNA, RNA, si-RNA), peptides and proteins [70].

However, delivering drugs to the lungs must contend with the presence of the airway surface layer (ASL), a hydrogel-like viscoelastic protective barrier that is excessively produced in obstructive lung diseases (CF and COPD) [71,72]. ASL comprises the upper mucus layer (ML), primarily composed of a mucin network, and the lower periciliary layer (PCL), which harbors membrane-spanning mucins and large mucopolysaccharides tethered to cilia, microvilli, and the epithelial surface [73]. The three-dimensional mesh of PCL mucins acts as a barrier, restricting the entry of both the ML and inhaled particles into the PCL milieu. Consequently, regardless of the various delivery systems under consideration [74], a successful therapeutic strategy necessitates drugs crossing the ASL, underscoring the critical importance of a deep understanding of the ASL hydrogel nanostructure. While traditional drugs typically have dimensions ranging from 1 to 10 nm [75], in many situations, particularly in gene delivery, drugs must be bound to carriers to protect them from environmental factors such as enzymes. The dimensions of these carriers vary from (20–50) nm (gold nanostars [69] and silver nanoparticles [76]) to (100−200) nm (liposomes [77]) and (300–600) nm (lipid particles [67,71]. Given that the mesh size of the polymeric network in the pathological CF mucus ranges from several tenths of nanometers up to approximately 300 nm [62], it becomes evident that ASL poses a significant hindrance to the diffusion of drug-carrier complexes towards target cells.

To get a quantitative grasp of this phenomenon, understanding the impact of meshwork size distribution on drug release or diffusion through ASL holds paramount importance. In general, as the ratio of solute radius to average mesh size (r_s/ζ_m) decreases, the effect of the distribution on the diffusion process is expected to diminish. However, our demonstration reveals that the distribution of diffusion coefficients, as governed by Weibull's statistics, consistently skews towards larger values compared to that Gaussian (SI 5.10). Considering the CF sputum sample of patient 178 as an example, this disparity remains minimal for small solutes ($r_s \approx 1$ nm) but becomes increasingly significant for larger solutes (50 % for $r_s \approx 20$ nm), a common occurrence in gene delivery where drugs are bound to carriers for protection against environmental factors such as enzymes. Furthermore, still when accounting for large

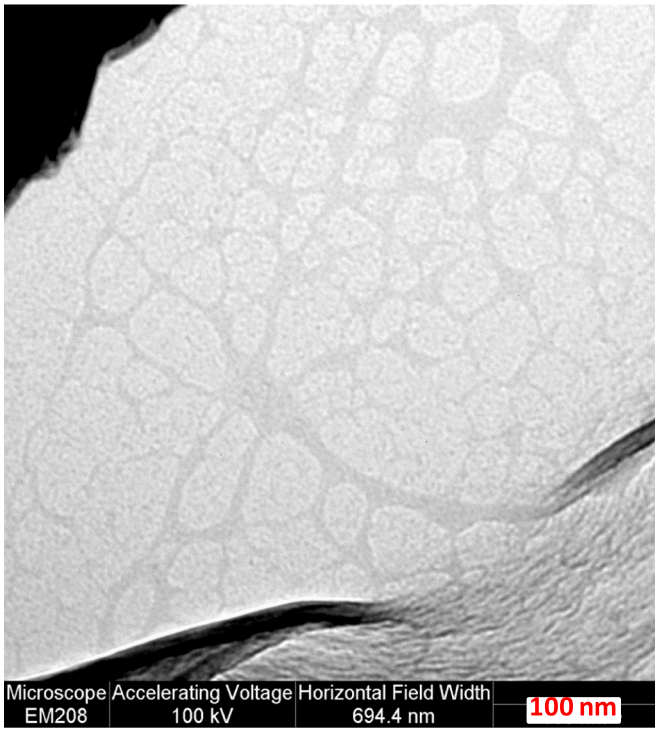

Fig. 10. Transmission electron microscopy (TEM) image of the PVP-K90 hydrogel, acquired using a Philips EM208 at 100 kV. The technical procedure followed to obtain this picture can be found in [63]. Gray ribbons indicate PVP chains bundles.

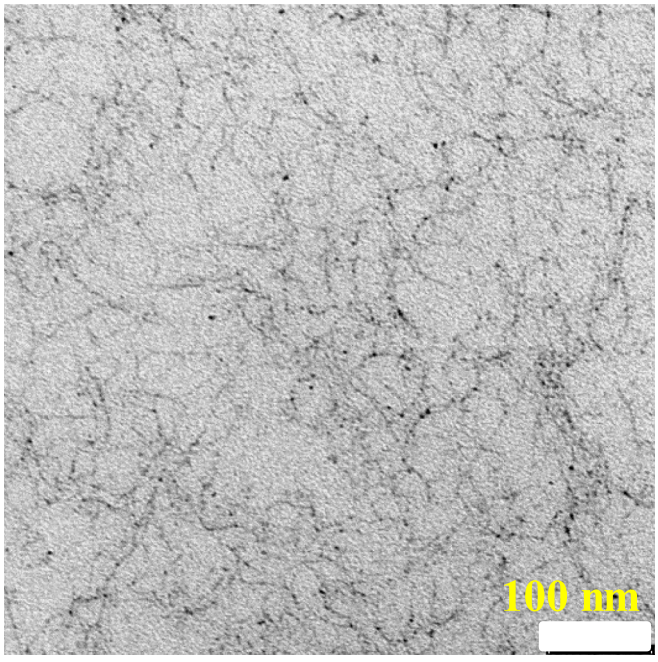

Fig. 11. TEM image referring to the alginate 2 % 3 g/l hydrogel (Philips EM208 100 kV). The technical procedure followed to obtain this picture can be found in [64]. Black lines indicate alginate chains.

solutes (r_s/ζ_m = 0.4–0.5), notable differences emerge between the Gaussian and generalized Weibullian, resulting in substantial disparities in solute diffusion: ASL exhibits significantly greater permeability to drug molecules with the generalized Weibull distribution, indicating that the concentration evolution under this condition remarkably precedes that derived from the Gaussian statistics (SI 5.10).

4.5. Impact in the study of transport properties: thermoplasmonic and photothermal applications

Along with the obvious repercussions on the study of gel materials and their bio–based applications, a couple of topics warrant further consideration. The first concerns the theoretical analysis of the thermal and thermomechanical properties of a polymer network. In particular, determining thermal conductivity – such as via the Green-Kubo approach – relies on the heat flux, which is governed by the configuration-space distribution of the polymer chains, and more precisely by the separation and interaction forces between monomer units, ultimately reflected in the stress tensor. It has been found that the thermal contribution of the polymer phase is predominantly influenced by non-bonded contacts, while energy transfer along bonds plays a comparatively minor role (see e.g. refs. [78, 79]). Given this, it would be interesting to examine how deviations from the Gaussian profile, expressible through the Weibull distribution, influence thermal behavior. On one hand, introducing stiffness sources in the polymer backbone, such as a transition from perfectly Hookean dumbbells to stiffened Fraenkel dumbbells, is associated with the emergence of negative contributions to thermal conductivity [80]. On the other hand, within a Debye model, thermal conductivity is proportional to a linear combination of bulk and shear moduli, which we have shown to be affected by the use of a Weibull distribution [78].

Secondly, a range of promising applications utilizes the photothermal or thermoplasmonic effect of metal nanoparticles, typically gold or silver. When subjected to appropriate laser irradiation, these nanoparticles can focus light down to nanometer scales (i.e. through plasmon waves), generating localized heating useful for applications such as chemical photosynthesis, or clinical hyperthermia therapy for cancer [81], to name a few. In thermochemotherapy, coupling nanoparticles with smart polymers or gels (e.g. alginate or agarose hydrogels) enables controlled heating to induce conformational changes in the macromolecular structure [82–84]. Now, it is clear that the spatial distribution of polymer chains in the matrix plays a crucial role in determining the heat transfer dynamics of plasmonic nanoparticles in the system. The polymer network creates a heterogeneous environment characterized by an average mesh size that affects local thermophysical properties and nanoparticle mobility. Heat transfer is affected in a number of ways: i.) Polymer chains determine the effective thermal conductivity of the gelled matrix. While water generally has a high thermal conductivity compared to polymers, a dense polymer network can introduce thermal resistance due to its lower conductivity. This resistance can lead to non-uniform heat dissipation, resulting in localized temperature gradients. ii.) If the network has highly entangled or densely crosslinked regions, these areas may impede heat diffusion, causing more significant temperature increases in localized zones where nanoparticles accumulate. Conversely, in loosely crosslinked regions with larger mesh sizes, heat may disperse more efficiently, leading to more uniform temperature profiles. iii). The polymer distribution also regulates water retention, which influences the heat capacity of the gel. A tighter network retains water more effectively, maintaining the overall cooling efficiency, while a looser network may permit more rapid evaporation, affecting the system's thermal response.

As thoroughly discussed in SI 5.10, diffusion of plasmonic nanoparticles in the gelled matrix is also closely tied to the spatial distribution of polymer chains, which determines the available free volume for particle motion. When the mesh size is comparable to or smaller than the nanoparticle diameter, steric hindrance limits mobility, leading to sub-diffusion, while larger mesh sizes promote normal diffusion. Nanoparticles may encounter regions with high polymer density that act as barriers, leading to restricted diffusion and potential accumulation. In contrast, less dense regions allow for enhanced transport. Photothermal heating of nanoparticles can also induce thermophoretic motion, where

particles migrate along temperature gradients. The extent of this movement depends on the polymer network ability to sustain temperature gradients. A highly crosslinked gel with poor heat dissipation normally elicits thermophoresis, bringing to clustering in heated areas. Ultimately, the arrangement of polymer chains in space modifies the hydrodynamic drag acting on nanoparticles, thereby affecting their effective diffusion.

A little more quantitatively, the (homogeneous) temperature difference between the nanoparticle surface and bulk phase (ΔT) arising from the thermoplasmonic effect – and the related photothermal efficiency – depends on quantities such as absorption cross–section (σ_a) and equivalent size (R_e), typically defined as the radius of a sphere with the same volume as the nanoparticle, multiplied by a coefficient that is slightly greater than unity. A basic relation for this phenomenology follows from Baffou's theory [85], where ΔT is proportional to $\approx \sigma_a I/(4\pi k_T R_e)$, where I is the light irradiance. The coefficient k_T denotes the thermal conductivity of the medium – here, the gel phase – affected, as previously described, by the conformational distribution of the polymer skeleton. Using a soft polymer phase instead of a liquid to host the thermoplasmonic effect ensures better homogeneity in the desired thermal activation process or treatment. Excessive heating may cause shrinkage of the hydrogel meshes, implying a transition in nanoparticle motion from diffusive to even superdiffusive [86]. Conversely, if nanoparticles are too immobilized within the gel, their heat transfer can be significantly hindered [87], as previously discussed.

5. Conclusions

The shift in paradigm, transitioning from Gaussian to Weibull's statistics, is poised to usher in new research opportunities across both addressed and unresolved polymer network problems. We have thoroughly examined the potential breadth of implications, yielding outcomes that are straightforward to apply and encompass a wide range: the classification of hydrogels within the realm of extreme value statistics, simple formulas for their mechanical moduli (elastic and shear) and the enhanced precision in inferring the mesh size in polysaccharide (agar, alginate, scleroglucan), sputum samples from cystic fibrosis patients and synthetic polymers (PVP-K90 and PEG-PPG), promising for more efficacious therapeutic strategies, also in the context of cancer treatment. Within such a spectrum, this transition will raise a number of intriguing questions, spanning from the quest for universal constitutive models and the study of thermomechanical properties, to the mimicry of cellular tissues (simulated by hybrid networks with diverse persistence lengths and mesh size scales), as well as the exploration of drug delivery mechanisms using hydrogels with nanoparticle carriers, the analysis of diseased tissues with characteristics similar to gels or biopolymer networks, and applications to photothermal or thermoplasmonic phenomena in a gelled matrix. Also, Gauss functions are recognized for their symmetry and bounded tails, while Weibullians can assume various shapes, including skewed distributions with heavy tails. This versatility is anticipated to render Weibull's laws viable for modelling an expanded array of phenomena. Also, what we can presently state with certainty is that none of the polymer networks we analyzed display a Gaussian end-to-end length distribution. Although these deviations may not always seem pronounced, they have meaningful consequences for the interpretation of microstructure, as demonstrated in our discussion of hydrogel mesh size. As detailed in SI 5.10, such deviations become especially relevant for the diffusion of large molecules – processes that critically impact mass and thermal transport. This stands among the most important practical conclusions of our study.

Among the open questions raised by our study, two stand out – one theoretical and one phenomenological. The first stems from the formal difficulties introduced by monomer correlations in the Weibull distribution, which necessitated approximating the configuration integrals and the corresponding mechanical responses in a series expansion of the parameter u (representing the forbidden region for small end-to-end polymer distances) and for small deformations ($\alpha \approx 1$), as required by experiments conducted in the linear regime. The treatment for arbitrary values of u and α likely requires an ad-hoc numerical computation, and therefore remains an open problem. Secondly, we applied the theory to distributions with a single peak, whereas it is known that some polymer networks exhibit (at least) bimodal end-to-end distributions. Addressing this case requires assessing whether a linear combination of Weibull functions is applicable. If so, the response could, to a reasonable approximation, result from the linear combination of contributions from each peak, where distinct energy concentrations take place. In a future study, we plan to test the applicability of our theory to bi– or n–modal distributions in the linear deformation regimes.

CRediT authorship contribution statement

Stefano A. Mezzasalma: Writing – review & editing, Writing – original draft, Validation, Methodology, Investigation, Formal analysis, Conceptualization. **Michela Abrami:** Writing – review & editing, Writing – original draft, Visualization, Validation, Methodology, Investigation, Data curation. **Gabriele Grassi:** Writing – review & editing, Validation, Methodology, Investigation, Formal analysis, Conceptualization. **Mario Grassi:** Writing – review & editing, Writing – original draft, Validation, Methodology, Investigation, Formal analysis, Conceptualization.

Declaration of competing interest

The authors declare that they have no known competing financial interests or personal relationships that could have appeared to influence the work reported in this paper.

Acknowledgement

This work was partly supported by the Croatian Science Foundation under the project number HRZZ-IP-2022-10-3456 (S.A.M). M.A, G.G and M.G thank the financial support of the Italian Ministry of Education (Finanziato dall'Unione europea – Next Generation EU, Missione 4 Componente 1, CUP J53D23002200006").

Appendix A. Supplementary data

Supplementary data to this article can be found online at https://doi.org/10.1016/j.ijbiomac.2025.144741.

References

[1] J. Li, D. Mooney, Designing hydrogels for controlled drug delivery, Nat. Rev. Mater. 1 (2016) 16071, https://doi.org/10.1038/natrevmats.2016.71.
[2] F. Mo, K. Jiang, D. Zhao, Y. Wang, J. Song, W. Tan, W., Dna hydrogel-based gene editing and drug delivery systems, Adv. Drug Deliv. Rev. 168 (2021) (2021) 79–98, https://doi.org/10.1016/j.addr.2020.07.018.
[3] M. Grassi, G. Grassi, Application of mathematical modeling in sustained release delivery systems, Expert Opin. Drug Deliv. 11 (8) (2014) 1299–1321, https://doi.org/10.1517/17425247.2014.924497.
[4] M. Castronovo, A. Lucesoli, P. Parisse, A. Kurnikova, A. Malhotra, M. Grassi, G. Grassi, B. Scaggiante, L. Casalis, G. Scoles, Two-dimensional enzyme diffusion in laterally confined DNA monolayers, Nat. Commun. 2 (2011) 297, https://doi.org/10.1038/ncomms1296.
[5] B. Amsden, Hydrogel mesh size and its impact on predictions of mathematical models of the solute diffusion coefficient, Macromolecules 55 (18) (2022) 8399–8408, https://doi.org/10.1021/acs.macromol.2c01443.
[6] X. Zhao, J. Kim, C.A. Cezar, N. Huebsch, K. Lee, K. Bouhadir, D.J. Mooney, Active scaffolds for ondemand drug and cell delivery, Proc. Natl. Acad. Sci. 108 (1) (2011) 67–72, https://doi.org/10.1073/pnas.1007862108.
[7] E. Calò, V.V. Khutoryanskiy, Biomedical applications of hydrogels: a review of patents and commercial products, Eur. Polym. J. 65 (2015) 252–267, https://doi.org/10.1016/j.eurpolymj.2014.11.024.
[8] A. Zelikin, C. Ehrhardt, A. Healy, Materials and methods for delivery of biological drugs, Nat. Chem. 8 (2016) 997–1007, https://doi.org/10.1038/nchem.2629.
[9] M. Jaspers, S. Vaessen, P. Schayik, D. Voerman, A. Rowan, P. Kouwer, Nonlinear mechanics of hybrid polymer networks that mimic the complex mechanical

environment of cells, Nat. Commun. 8 (2017) 15478, https://doi.org/10.1038/ncomms15478.
[10] M. Zhong, R. Wang, K. Kawamoto, B.D. Olsen, J.A. Johnson, Quantifying the impact of molecular defects on polymer network elasticity, Science 353 (2016) 1264–1268, https://doi.org/10.1126/science.aag0184.
[11] N.R. Richbourg, N.A. Peppas, The swollen polymer network hypothesis: quantitative models of hydrogel swelling, stiffness, and solute transport, Prog. Polym. Sci. 105 (2020) 101243, https://doi.org/10.1016/j.progpolymsci.2020.101243.
[12] M. Rubinstein, R. Colby, Polymer physics Chapt. 7, Oxford University Press, Oxford, 2003, https://doi.org/10.1093/oso/9780198520597.001.0001.
[13] C. Storm, J. Pastore, F. Mackintosh, T. Lubensky, P. Janmey, Nonlinear elasticity in biological gels, Nature 435 (2005) 191–194, https://doi.org/10.1038/nature03521.
[14] J. Wang, D. Lű, D. Mao, M. Long, Mechanomics: an emerging field between biology and biomechanics, Protein Cell 5 (7) (2014) 518–531, https://doi.org/10.1007/s13238-014-0057-9.
[15] J. Humphrey, Review paper: continuum biomechanics of soft biological tissues, Proc. R. Soc. Lond. Ser. A Math. Phys. Eng. Sci. 459 (2029) (2003) 3–46, https://doi.org/10.1098/rspa.2002.1060.
[16] S. Lenzini, R. Bargi, G. Chung, J.W. Shin, Matrix mechanics and water permeation regulate extracellular vesicle transport, Nat. Nanotechnol. 15 (2020) 217–223, https://doi.org/10.1038/s41565-020-0636-2.
[17] P. Flory, Principles of Polymer Chemistry. Baker Lectures 1948 Chapt. XI, Cornell University Press, Ithaca, New York, USA, 1953.
[18] S.A. Mezzasalma, M. Abrami, M. Grassi, G. Grassi, Rubber elasticity of polymer networks in explicitly non-gaussian states. Statistical mechanics and lf-nmr inquiry in hydrogel systems, Int. J. Eng. Sci. 176 (2022) 103676, https://doi.org/10.1016/j.ijengsci.2022.103676.
[19] E. Bertin, Global fluctuations and gumbel statistics, Phys. Rev. Lett. 95 (2005) 170601, https://doi.org/10.1103/PhysRevLett.95.170601.
[20] E. Bertin, M. Clusel, Generalized extreme value statistics and sum of correlated variables, J. Phys. A Math. Gen. 39 (24) (2006) 7607, https://doi.org/10.1088/0305-4470/39/24/001.
[21] J.F. Pinton, P.C.W. Holdsworth, R. Labbe, Power fluctuations in a closed turbulent shear flow, Phys. Rev. E 60 (1999) 2452–2455, https://doi.org/10.1103/PhysRevE.60.R2452.
[22] S.T. Bramwell, J.Y. Fortin, P.C.W. Holdsworth, S. Peysson, J.F. Pinton, B. Portelli, M. Sellitto, Magnetic fluctuations in the classical XY model: the origin of an exponential tail in a complex system, Phys. Rev. E 63 (2001) 041106, https://doi.org/10.1103/PhysRevE.63.041106.
[23] A. Comtet, P. Leboeuf, S.N. Majumdar, Level density of a bose gas and extreme value statistics, Phys. Rev. Lett. 98 (2007) 070404, https://doi.org/10.1103/PhysRevLett.98.070404.
[24] S.T. Bramwell, K. Christensen, J.Y. Fortin, P.C.W. Holdsworth, H.J. Jensen, S. Lise, J.M. Lopez, M. Nicodemi, J.F. Pinton, M. Sellitto, Universal fluctuations in correlated systems, Phys. Rev. Lett. 84 (2000) 3744–3747, https://doi.org/10.1103/PhysRevLett.84.3744.
[25] T. Antal, M. Droz, G. Gyorgyi, Z. Racz, 1/f noise and extreme value statistics, Phys. Rev. Lett. 87 (2001) 240601, https://doi.org/10.1103/PhysRevLett.87.240601.
[26] S. Joubaud, A. Petrosyan, S. Ciliberto, N.B. Garnier, Experimental evidence of non-gaussian fluctuations near a critical point, Phys. Rev. Lett. 100 (2008) 180601, https://doi.org/10.1103/PhysRevLett.100.180601.
[27] C. Chamon, P. Charbonneau, L.F. Cugliandolo, D.R. Reichman, M. Sellitto, Out-of-equilibrium dynamical fluctuations in glassy systems, J. Chem. Phys. 121 (20) (2004) 10120–10137, https://doi.org/10.1063/1.1809585.
[28] J. Sievers, V. Mahajan, P.B. Welzel, C. Werner, A. Taubenberger, Precision hydrogels for the study of cancer cell mechanobiology, Adv. Healthc. Mater. 12 (14) (2023) 2202514, https://doi.org/10.1002/adhm.202202514.
[29] S.A. Mezzasalma, J. Kruse, S. Merkens, E. Lopez, A. Seifert, R. Morandotti, M. Grzelczak, Light-driven self-oscillation of thermoplasmonic nanocolloids, Adv. Mater. 35 (41) (2023) e2302987, https://doi.org/10.1002/adma.202302987.
[30] A. Rao, A.S. Iglesias, M. Grzelczak, Choreographing oscillatory hydrodynamics with dna-coated gold nanoparticles, J. Am. Chem. Soc. 146 (27) (2024) 18236–18240, https://doi.org/10.1021/jacs.4c06868.
[31] P. Farrell, The prevalence of cystic fibrosis in the European Union, J. Cyst. Fibros. 7 (2008) 450–453, https://doi.org/10.1016/j.jcf.2008.03.007.
[32] M. Abrami, M. Maschio, M. Conese, M. Confalonieri, F. Salton, F. Gerin, B. Dapas, R. Farra, A. Adrover, G. Milcovich, C. Fornasier, A. Biasin, M. Grassi, G. Grassi, Effect of chest physiotherapy on cystic fibrosis sputum nanostructure: an experimental and theoretical approach, Drug Deliv. Transl. Res. 12 (2022) 1943–1958, https://doi.org/10.1007/s13346-022-01131-8.
[33] O. Ciofu, T. Tolker-Nielsen, P. Østrup Jensen, H. Wang, N. Hby, Antimicrobial resistance, respiratory tract infections and role of biofilms in lung infections in cystic fibrosis patients, Adv. Drug Deliv. Rev. 85 (2015) (2015) 7–23, https://doi.org/10.1016/j.addr.2014.11.017.
[34] L.R.G. Treloar, The Physics of Rubber Elasticity, 3rd edition, Clarendon Oxford, Oxford, 1975.
[35] E.N. Arruda, M.C. Boyce, M.C. A, A three-dimensional constitutive model for the large stretch behavior of rubber elastic materials, J. Mech. Phys. Solids 41 (2) (1993) 389–412, https://doi.org/10.1016/0022-5096(93)90013-6.
[36] B. Erman, P.J. Flory, Relationships between stress, strain, and molecular constitution of polymer networks. Comparison of theory with experiments, Macromolecules 15 (3) (1982) 806–811, https://doi.org/10.1021/ma00231a023.
[37] J.-Y. Fortin, M. Clusel, Applications of extreme value statistics in physics, J. Phys. A Math. Theor. 48 (18) (2015) 183001, https://doi.org/10.1088/1751-8113/48/18/183001.
[38] M. Clusel, E. Bertin, Global fluctuations in physical systems: a subtle interplay between sum and extreme value statistics, Int. J. Mod. Phys. B 22 (20) (2008) 3311–3368, https://doi.org/10.1142/S021797920804853X.
[39] W.K. Brown, K.H. Wohletz, Derivation of the Weibull distribution based on physical principles and its connection to the Rosin–Rammler and lognormal distributions, J. Appl. Phys. 78 (4) (1995) 2758–2763, https://doi.org/10.1063/1.360073.
[40] Hughes, (Chapt. 7): The self-avoiding walk, in: Random Walks and Random Environments. Vol. 1: Random Walks, Oxford Science Publications, Clarendon Press, 1995.
[41] S.A. Mezzasalma, Macromolecules in solution and brownian relativity, Interface Sci. Technol. 15 (2008) 1–236, https://doi.org/10.1016/S1573-4285(07)00009-9.
[42] S.N. Majumdar, A. Pal, G. Schehr, Extreme value statistics of correlated random variables: a pedagogical review, Phys. Rep. 840 (2020) 1–32, https://doi.org/10.1016/j.physrep.2019.10.005.
[43] P. Matricardi, F. Alhaique, T. Coviello, Polysaccahride Hydrogels: Characterization and Biomedical Applications, CRC Press, Boca Raton, USA, 2016, p. 540. Taylor & Francis Group.
[44] M. Abrami, F. Bignotti, F. Baldi, G. Spagnoli, A. Biasin, L. Grassi, G. Grassi, M. Grassi, Rheological and low field NMR characterization of hydrophobically-modified PEG hydrogels for drug delivery, Int. J. Pharm. 637 (2023) 122882, https://doi.org/10.1016/j.ijpharm.2023.122882.
[45] P. Marizza, M. Abrami, S.S. Keller, P. Posocco, E. Laurini, K. Goswami, A.L. Skov, A. Boisen, D. Larobina, G. Grassi, M. Grassi, Synthesis and characterization of UV photocrosslinkable hydrogels with poly(N-vinyl-2-pyrrolidone): determination of the network mesh size distribution, Int. J. Polym. Mater. Polym. Biomater. 65 (2016) 516–525, https://doi.org/10.1080/00914037.2015.1129964.
[46] S. Meiboom, D. Gill, Modified spin-echo method for measuring nuclear relaxation times, Rev. Sci. Instrum. 29 (8) (1958) 688–691, https://doi.org/10.1063/1.1716296.
[47] K.P. Whittal, A.L. MacKay, Quantitative interpretation of NMR relaxation data, J. Magn. Reson. 84 (1989) 134–152, https://doi.org/10.1016/0022-2364(89)90011-5.
[48] S.W.A. Provencher, A constrained regularization method for inverting data represented by linear algebraic or integral equations, Comput. Phys. Commun. 27 (1982) 213–227, https://doi.org/10.1016/0010-4655(82)90173-4.
[49] X. Wang, Q. Ni, Determination of cortical bone porosity and pore size distribution using a low field pulsed NMR approach, J. Orthop. Res. 21 (2003) 312–319, https://doi.org/10.1016/S0736-0266(02)00157-2.
[50] M.M. Chui, R.J. Phillips, M.J. McCarthy, Measurement of the porous microstructure of hydrogels by nuclear magnetic resonance, J. Colloid Interface Sci. 174 (2) (1995) 336–344, https://doi.org/10.1006/jcis.1995.1399.
[51] G.W. Scherer, Hydraulic radius and mesh size of gels, J. Sol-Gel Sci. Techn. 1 (1994) 285–291, https://doi.org/10.1007/BF00486171.
[52] M. Abrami, G. Chiarappa, R. Farra, G. Grassi, P. Marizza, M. Grassi, M. Use, Use of low field NMR for the characterization of gels and biological tissues, ADMET DMPK 6 (2018) 34–46, https://doi.org/10.5599/admet.6.1.430.
[53] T. Kopač, M. Abrami, M. Grassi, A. Ručigaj, M. Krajnc, Polysaccharide-based hydrogels crosslink density equation: a rheological and LF-NMR study of polymer-polymer interactions, Carbohydr. Polym. 277 (118895) (2022) 1–15.
[54] M. Holz, S.R. Heil, A. Sacco, Temperature-dependent self-diffusion coefficients of water and six selected molecular liquids for calibration in accurate 1H NMR PFG measurements, Phys. Chem. Chem. Phys. 2 (2000) 4740–4742, https://doi.org/10.1039/B005319H.
[55] R. Lapasin, S. Pricl, Rheology of industrial polysaccharides: theory and applications, Springer, New York, NY, 1995, https://doi.org/10.1007/978-1-4615-2185-3.
[56] G. Staltari, A. Biasin, L. Grassi, F. Gerin, M. Maschio, M. Confalonieri, M. Grassi, G. Grassi, M. Abrami, Rheological and low field NMR characterisation of cystic fibrosis patient's sputum, Chem. Biochem. Eng. Q. 36 (4) (2022) 239–253, https://doi.org/10.15255/CABEQ.2022.2119.
[57] N.R. Draper, H. Smith, Applied regression analysis, John Wiley & Sons Inc., New York, 1966.
[58] E. Pasut, R. Toffanin, D. Voinovich, C. Pedersini, E. Murano, M. Grassi, Mechanical and diffusive properties of homogeneous alginate gels in form of particles and cylinders, J. Biomed. Mater. Res. 87A (3) (2008) 808–818, https://doi.org/10.1002/jbm.a.31680.
[59] K.P. Burnham, D.R. Anderson, Model selection and multimodel inference a practical information-theoretic approach, Springer, New York, 2002.
[60] A. Grosberg, A. Yu, A.R. Khokhlov, Statistical Physics of Macromolecules chapt. 1,4, AIP Press, Melville, New York, 1994.
[61] J. Schurz, Rheology of polymer solutions of the network type, Prog. Polym. Sci. 16 (1) (1991) 1–53, https://doi.org/10.1016/0079-6700(91)90006-7.
[62] J.S. Suk, S.K. Lai, Y.Y. Wang, L.M. Ensign, P.L. Zeitlin, M.P. Boyle, J. Hanes, The penetration of fresh undiluted sputum expectorated by cystic fibrosis patients by non-adhesive polymer nanoparticles, Biomaterials 30 (13) (2009) 2591–2597, https://doi.org/10.1016/j.biomaterials.2008.12.076.
[63] G. Fanesi, M. Abrami, F. Zecchin, I. Giassi, E. Dal Ferro, A. Boisen, G. Grassi, P. Bertoncin, M. Grassi, P. Marizza, Combined use of rheology and LF-NMR for the characterization of PVP-alginates gels containing liposomes, Pharm. Res. 35 (2018) (2018) 171, https://doi.org/10.1007/s11095-018-2427-0.
[64] M. Abrami, I. D'Agostini, G. Milcovich, S. Fiorentino, R. Farra, F. Asaro, R. Lapasin, G. Grassi, M. Grassi, Physical characterization of alginate–Pluronic F127 gel for

endoluminal NABDs delivery, Soft Matter 10 (2014) (2014) 729–737, https://doi.org/10.1039/C3SM51873F.
[65] N.R. Richbourg, N.A. Peppas, High-throughput frap analysis of solute diffusion in hydrogels, Macromolecules 54 (22) (2021) 10477–10486, https://doi.org/10.1021/acs.macromol.1c01752.
[66] M.E. Taghavizadeh Yazdi, M. Qayoomian, S. Beigoli, M.H. Boskabady, Recent advances in nanoparticle applications in respiratory disorders: a review, Front. Pharmacol. 14 (2023), https://doi.org/10.3389/fphar.2023.1059343.
[67] A.Y. Lee, M.-H. Cho, S. Kim, Recent advances in aerosol gene delivery systems using non-viral vectors for lung cancer therapy, Expert Opin. Drug Deliv. 16 (7) (2019) 757–772, https://doi.org/10.1080/17425247.2019.1641083.
[68] C.M. Zimmermann, D. Baldassi, K. Chan, N.B. Adams, A. Neumann, D.L. Porras-Gonzalez, X. Wei, N. Kneidinger, M.G. Stoleriu, G. Burgstaller, D. Witzigmann, P. Luciani, O.M. Merkel, Spray drying sirna-lipid nanoparticles for dry powder pulmonary delivery, J. Control. Release 351 (2022) 137–150, https://doi.org/10.1016/j.jconrel.2022.09.021.
[69] M. Abrami, A. Biasin, F. Tescione, D. Tierno, B. Dapas, A. Carbone, G. Grassi, M. Conese, S. Di Gioia, D. Larobina, M. Grassi, Mucus structure, viscoelastic properties, and composition in chronic respiratory diseases, Int. J. Mol. Sci. 25 (2024) 1933, https://doi.org/10.3390/ijms25031933.
[70] Y. Liu, U.K. Sukumar, N. Jugniot, S.M. Seetharam, A. Rengaramachandran, N. Sadeghipour, P. Mukherjee, A. Krishnan, T.F. Massoud, R. Paulmurugan, Inhaled gold nano-star carriers for targeted delivery of triple suicide gene therapy and therapeutic micrornas to lung metastases: development and validation in a small animal model, Adv. Ther. 5 (8) (2022) 2200018, https://doi.org/10.1002/adtp.202200018.
[71] M. Puccetti, M. Pariano, C. Stincardini, P. Wojtylo, A. Schoubben, E. Nunzi, M. Ricci, L. Romani, S. Giovagnoli, S., Pulmonary drug delivery technology enables anakinra repurposing in cystic fibrosis, J. Control. Release 353 (2023) (2023) 1023–1036, https://doi.org/10.1016/j.jconrel.2022.11.043.
[72] T. Sonntag, M. Rapp, P. Didier, L. Lebeau, F. Pons, A. Casset, Mucus-producing epithelial models for investigating the activity of gene delivery systems in the lung, Int. J. Pharm. 614 (2022) 121423, https://doi.org/10.1016/j.ijpharm.2021.121423.
[73] M.M. Anjum, K.K. Patel, S. Bhattacharya, D.K. Arya, P. Pandey, P.M. R, S. Singh, P. S. Rajinikanth, Overcoming barriers in cystic fibrosis therapy through inhalational lipid nanoparticles: challenges and advances, J. Drug Deliv. Sci. Technol. 9 (2023) 105068, https://doi.org/10.1016/j.jddst.2023.105068.
[74] B. Button, L.H. Cai, C. Ehre, M. Kesimer, D. Hill, J. Sheehan, R. Boucher, M. Rubinstein, A periciliary brush promotes the lung health by separating the mucus layer from airway epithelia, Science 337 (2012) 937–941, https://doi.org/10.1126/science.1223012.
[75] M. Grassi, G. Grassi, R. Lapasin, I. Colombo, Understanding drug release and absorption mechanisms: a physical and mathematical approach, CRC press, Boca Raton, 2006, https://doi.org/10.1201/9781420004656.
[76] S. Rano, A. Bhaduri, M. Singh, Nanoparticle-based platforms for targeted drug delivery to the pulmonary system as therapeutics to curb cystic fibrosis: a review, J. Microbiol. Methods 217-218 (2024) 106876, https://doi.org/10.1016/j.mimet.2023.106876.
[77] R. Ghanem, M. Berchel, T. Haute, X. Buin, V. Laurent, R. Youf, A. Bouraoui, T. Le Gall, P.A. Jaffres, T. Montier, Gene transfection using branched cationic amphiphilic compounds for an aerosol administration in cystic fibrosis context, Int. J. Pharm. 631 (2023) 122491, https://doi.org/10.1016/j.ijpharm.2022.122491.
[78] D. Mukherji, Thermal conductivity of polymers: a simple matter where complexity matters, Macromol. Rapid Commun. 45 (24) (2024), https://doi.org/10.1002/marc.202400517.
[79] M. An, B. Demir, X. Wan, H. Meng, N. Yang, T.R. Walsh, Predictions of thermo-mechanical properties of cross-linked polyacrylamide hydrogels using molecular simulations, Adv. Theory Simul. 2 (2) (2019) 1800153, https://doi.org/10.1002/adts.201800153.
[80] C.F. Curtiss, R.B. Bird, Thermal conductivity of dilute solutions of chainlike polymers, J. Chem. Phys. 107 (12) (1997) 5254, https://doi.org/10.1063/1.474888.
[81] P.R. Stauffer, Evolving technology for thermal therapy of cancer, Int. J. Hyperth. 21 (7) (2005) 731–744, https://doi.org/10.1080/02656730500331868.
[82] L.-H. Tsai, T.-H. Young, C.-H. Yen, W.-C. Yao, C.-H. Chang, Intratumoral thermo-chemotherapeutic alginate hydrogel containing doxorubicin-loaded PLGA nanoparticle and heating agent, Int. J. Biol. Macromol. 251 (2023) 126221, https://doi.org/10.1016/j.ijbiomac.2023.126221.
[83] S. Lee, S. Kim, D. Kim, J. You, J.S. Kim, H. Kim, J. Park, J. Song, J. Choi, Spatiotemporally controlled drug delivery via photothermally driven conformational change of self-integrated plasmonic hybrid nanogels, J. Nanobiotechnol. 21 (2023) 191, https://doi.org/10.1186/s12951-023-01935-x.
[84] L. Moretti, A. Mazzanti, A. Rossetti, A. Schirato, L. Polito, F. Pizzetti, A. Sacchetti, G. Cerullo, G. Della Valle, F. Rossi, M. Maiuri, Plasmonic control of drug release efficiency in agarose gel loaded with gold nanoparticle assemblies, Nanophotonics *10* (1) (2021) 247–257, https://doi.org/10.1515/nanoph-2020-0418 (2021).
[85] G. Baffou, R. Quidant, F.J. Garcìa de Abajo, Nanoscale control of optical heating in complex plasmonic systems, ACS Nano 4 (2) (2010) 709, https://doi.org/10.1021/nn901144d.
[86] N. Carl, J. Sindram, M. Gallei, S.U. Egelhaaf, M. Karg, From normal diffusion to superdiffusion: Photothermal heating of plasmonic core-shell microgels, Phys. Rev. E 100 (5) (2019) 052605, https://doi.org/10.1103/PhysRevE.100.052605.
[87] U.M. Engelmann, J. Seifert, B. Mues, S. Roitsch, C. Ménager, A.M. Schmidt, I. Slabu, Heating efficiency of magnetic nanoparticles decreases with gradual immobilization in hydrogels, J. Magn. Magn. Mater. 471 (2019) 486–494, https://doi.org/10.1016/j.jmmm.2018.09.113.